

C-CLASS CATAMARAN WING PERFORMANCE OPTIMISATION

A THESIS SUBMITTED TO THE UNIVERSITY OF MANCHESTER
FOR THE DEGREE OF MASTER OF PHILOSOPHY
IN THE FACULTY OF ENGINEERING AND PHYSICAL SCIENCES

2011

By
Nils Haack
School of Mechanical, Aerospace and Civil Engineering

Contents

Abstract	5
Declaration	6
Acknowledgements	8
1 Introduction	9
1.1 Aims	11
1.2 Objectives	12
2 Literature Review	13
2.1 Wingsails	13
2.1.1 C-Class Catamaran development - the history of the class	13
2.1.2 Wingsail occurrence in other sailing classes	16
2.1.3 Wingsail research	16
2.2 Physics of sailing	20
2.2.1 Wind: velocity variations with height	20
2.2.2 Apparent wind	21
2.2.3 Righting moment	23
2.2.4 Forces on a boat	24
2.2.5 Boat performance requirement for fleet and match racing .	26
2.2.6 Sailing upwind	26
2.2.7 Downwind sailing	28
2.2.8 Summary of wingsail requirements for a C-Class catamaran	29
2.3 Computational Fluid Dynamics (CFD)	30
2.3.1 Governing equations	30
2.4 Near wall flows	31
2.4.1 Flow physics	31

2.4.2	Modelling of the near wall flows	32
2.4.3	Grid requirements	34
2.5	Turbulence modelling	35
2.5.1	Reynolds Average Navier-Stokes (RANS)	36
2.5.2	Reynolds stresses	37
2.5.3	The $k - \epsilon$ model	39
2.5.4	The SST $k - \omega$ model	40
2.5.5	Choosing a turbulence model	40
2.6	Finite volume method	42
2.6.1	Interpolation	43
2.6.2	Discretisation	44
2.7	Mesh	45
2.7.1	Aerofoil meshing	45
2.8	Conclusion of Literature Review	46
3	Methods	47
3.1	Description of problem	47
3.2	The wing	48
3.2.1	Wing setup and use	50
3.3	Modelling requirements	51
3.3.1	Tackling the modelling requirements	51
3.4	2D mesh generation	52
3.5	2D simulation setup	58
3.5.1	Considerations	58
3.6	3D Mesh Generation	60
3.6.1	Wing Mesh	60
3.6.2	Wing with Boat Mesh	63
3.7	3D Simulation Setup	65
4	Results and Analysis	66
4.1	2D Simulations	66
4.1.1	Polars	66
4.1.2	Gap Effect	68
4.1.3	Effect of discretisation scheme	72
4.2	Remarks about the turbulence models	74
4.3	Further analysis of Profile data	74

4.4	IC ⁴ 2010 - the race	74
4.5	3D wing results and analysis	76
4.6	Conclusion	78
4.7	Figures	79
5	Future work	82
5.1	Turbulence model selection	82
5.1.1	Turbulence of wind	82
5.2	Separated flow cases	82
5.3	Point of separation	83
5.4	Flap leading edge location	83
5.5	Root wing tip gap size	83
5.6	Wing/Chord ratio	83
5.7	Wing profile analysis	83
5.8	Wingsail twist	84
5.9	6-degree-of-freedom simulation	84
	Appendices	88
A	Terms used in sailing	89
B	Historical background of sailing	90
B.1	From drag to lift	90
B.2	From sail to wingsail	91
C	Hydrofoils in the C-Class	94
D	Structured o-mesh	96
E	NACA 0012 profile results and analysis	97
E.1	Mesh comparison	97
E.2	Turbulence model comparison	99
E.3	Conclusion	101
F	Simulation setup	102
F.1	Explanation of choice of physical models	102
F.2	Boundary condition	103
F.3	Initial condition	103

Abstract

This research is concerned with the wing of the C-Class catamaran of Team Invictus. The current wing is a reverse engineered design of a previously successful C-Class catamaran; a wing with an external flap. This design was modified at the trailing edge of the main wing with a morphing trailing edge. The modifications were done on the basis of engineering judgements. Due to budget restrictions expensive wind tunnel tests were not conducted. Thus results of this study are not compared to wind tunnel tests.

Within the limits of this degree lift and drag polars (in this case a polar is the lift coefficient C_l or drag coefficient C_d plotted versus the angle of attack) of the wing profile were produced. This was done by the use of CFD (Computational Fluid Dynamics). The standard $k - \epsilon$ turbulence model was concluded to be sufficient for this task.

It was found that a 2% (of main wing chord) gap setting between the trailing edge of the main wing section and the flap is more efficient than the previously used 3%.

Further more a flow visualisation study was conducted around the entire wing. The visualisation indicates that the boat hull has an effect on the pressure distribution on the wing and that more detailed analysis is required to quantify the effects of the gap between the root of the wing and the boat.

Declaration

- i The author of this thesis (including any appendices and/or schedules to this thesis) owns certain copyright or related rights in it (the "Copyright") and s/he has given The University of Manchester certain rights to use such Copyright, including for administrative purposes.
- ii Copies of this thesis, either in full or in extracts and whether in hard or electronic copy, may be made **only** in accordance with the Copyright, Designs and Patents Act 1988 (as amended) and regulations issued under it or, where appropriate, in accordance with licensing agreements which the University has from time to time. This page must form part if any such copies made.
- iii The ownership of certain Copyright, patents, designs, trade marks and other intellectual property (the "Intellectual Property") and any reproductions of copyright works in the thesis, for example graphs and tables ("Reproductions"), which may be described in this thesis, may not be owned by the author and may be owned by third parties. Such Intellectual Property and Reproductions cannot and must not be made available for use without the prior written permission of the owner(s) of the relevant Intellectual Property and/or Reproductions.
- iv Further information on the conditions under which disclosure, publication and commercialisation of this thesis, the Copyright and any Intellectual Property and/or Reproductions described in it may take place is available in the University IP Policy (see <http://www.campus.manchester.ac.uk/medialibrary/policies/intellectual-property.pdf>), in any relevant Thesis restriction declarations deposited in the University Library, The University Library's regulations (see <http://www.manchester.ac.uk/>

[library/aboutus/regulations](#)) and in The University's policy on presentation of Thesis.

Acknowledgements

I would like to thank Dr. Dala for giving me the opportunity to pursue this degree. I want to thank Team Invictus and especially Julien Chaussée for providing the data for this project and constructive conversations throughout the project. I also like to thank my supervisor Dr. Prosser for his invaluable help and guidance.

Chapter 1

Introduction

This research is concerned with the wing used to propel the C-Class catamaran of the British Team Invictus (see figure 1.1). The C-Class is a development class; this means that the design of the boats is only restricted by a few rules, giving room for development.



Figure 1.1: The current boat of Team Invictus, Invictus II [12]

Due to only a few design restrictions in this class, the development of the power unit led to the use of wings (to produce the drive force of the boat) rather than conventional soft sails. The C-Class competes currently in the IC^4 (International C-Class Catamaran Challenge). This competition is similar to the ‘America’s Cup’; hence it is often called the ‘Little America’s Cup’. The challenge is held in fleet and match races around a set course. In fleet races more than two boats compete around a set course. In a match race two boats compete typically around only two marks (one upwind mark and one downwind mark). The next challenge was at the New York Yacht Club in September 2010 [12].

Team Invictus reverse engineered their current wing from the wing of the boat ‘Cogito’. Cogito is a C-Class catamaran successful in the previous IC^4 s. Team Invictus modified the design to improve the aerodynamic properties. The modification is a morphing trailing edge of the main wing. This however was not done by aerodynamic analysis of the wing, it was a pure engineering judgement.

No aerodynamic data is available for this wing

Due to the limited funds available for the team, wind-tunnel test data are not available. The aim of this project, is to establish lift and drag polars (in this case a polar is the lift coefficient C_l or drag coefficient C_d plotted versus the angle of attack) of the wing profile. This will be done by the use of CFD (Computational Fluid Dynamics) simulations in place of experiments.

For a race yacht it is crucial to know the wing setup for the most efficient tacking-angle to go up wind and gybing-angle to go down wind. Tacking is changing the direction from one heading by turning the bow (front of a boat) through the wind to a different heading. This method is used for going up-wind. The tacking-angle is the angle between the two different headings. Gybing is changing directions by turning the stern (rear of a boat) through the wind. Hence gybing-angle is the angle between those two different headings. Finding those angles is currently done by a VPP (Velocity Prediction Programme), that considers the hydrodynamic and aerodynamic forces of the boat in order to predict the velocity of the boat in a polar. A velocity polar of a boat visualises the possible speed of a boat for every possible heading at constant wind velocity. A VPP is being developed by a third party.

The development of a VPP requires the evaluation of the forces that are generated by the wing. For the lift evaluation of the wing the lift distribution needs to be computed. However it is uncertain how the lift distribution is effected

by the gap between the boat and the root of the wing. Figure 1.2 shows two different scenarios of the lift distribution. One where the lift distribution is not effected (a) and one where the lift distribution is effected (b).

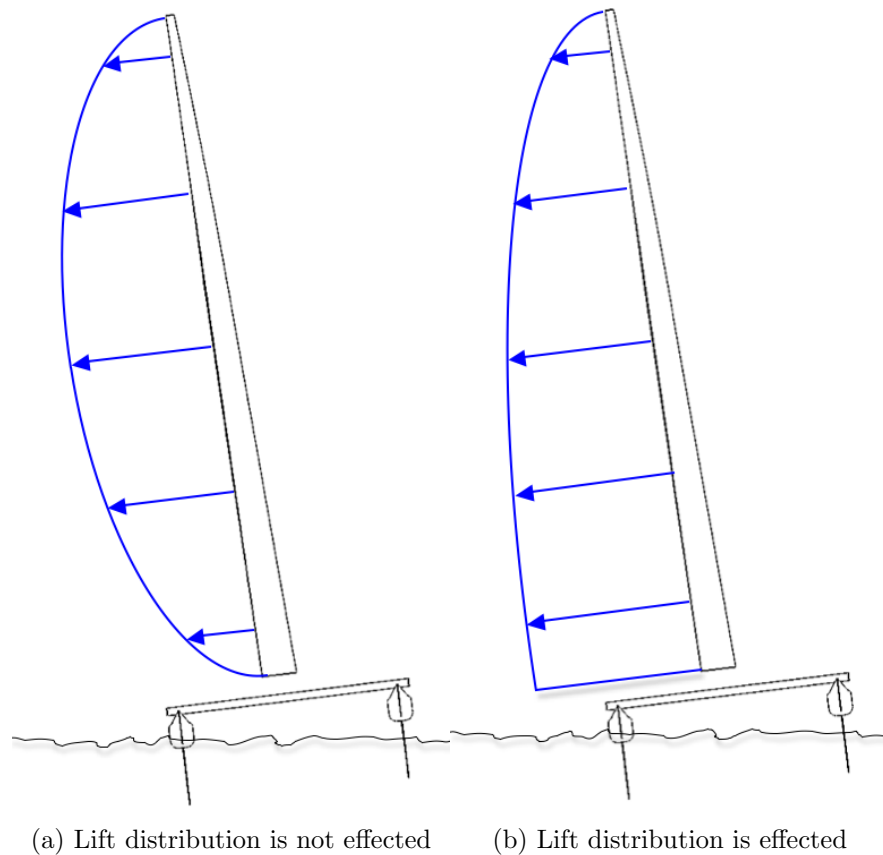


Figure 1.2: Lift distribution on the wing (indicated in blue) based on two different assumptions.

The current assumption is that the gap between the root of the wing and the water surface and the hull itself does not affect the vortex and subsequently the lift generated by the wing. A flow visualisation is required to indicate whether a more detailed analysis of this is required.

1.1 Aims

The aim of this study is to generate aerodynamic data required by the VPP. More precisely the lift and drag polars for the wing profile are sought in typical sailing

configurations. Furthermore, the effect of the gap size between the main wing and the flap on the polar plots is a key outcome.

Finally, visualisation of the flow around the root of the wing will be provided: this is intended to aid quantitative judgement on the effect on lift produced by a flying hull.

1.2 Objectives

In order to achieve the aims the following points need to be considered.

- Mesh sensitivity study
- Turbulence model selection
- Generate lift and drag polars with 2D CFD simulations
- Compare polar plots with different gap settings
- Visualise the flow around the wing and boat with 3D CFD simulations
- Determine whether further investigation of the flow around the root is required for the design of future wingsails.

Chapter 2

Literature Review

2.1 Wingsails

This chapter describes the relevant information regarding the wingsail under investigation. This includes an overview of the class, the developments in wing sailing, the sailing principles that drive the wing design and the computational methods used in CFD. Appendix A gives an explanation of words used in sailing. In Appendix B, the development in sailing throughout history is described, with a focus on how the C-Class is different from other sailing classes.

2.1.1 C-Class Catamaran development - the history of the class

With the establishment of the C-Class a set of rules was agreed upon. The C-Class is currently not recognised by the ISAF (International Sailing Federation) [10], the rules are currently published by the International C-Class Catamaran Association [12]. Those class rules are as following:

- Length: 25ft
- Beam: 14ft
- Sail area: 300sq ft
- Measured sail area to include the area of the mast and boom
- Crew: 2 trapeze (trapeze is a wire securing the crew while leaning backwards out over the hull)

- Mirror image hulls (hulls are the buoyant bodies of a boat. The C-Class is a catamaran class with two hulls)
- No minimum weight

The class sails in winds of up to 20 knots.

The first race in 1961 was won by the British with the catamaran ‘Hellcat’ against the American ‘Wildcat 300’. Hellcat had a fully battened main sail (battens are rigid enforcements running from the luff to the leach). The luff is the upwind edge of a sail and the leach is the downwind edge of a sail. This increased the stability of the profile of the sail. The next breakthrough design came with ‘Lady Helmsman’ in 1966. This catamaran had a wing shaped masted that holds over a quarter of the sail area. This catamaran was also the first with a una rig (main sail behind mast without gib) compared to the previous sloop rig (single mast with main sail and gib). In 1974 the first solid wing (wingsail) made its appearance with ‘Miss Nylex’. Since the introduction of the wingsail, a soft sail has only won one single race in this class, which was believed to be due to the lightness of the soft sail compared to the aerodynamically more advanced but heavier wingsail.

Over the years, various wing-flap configurations have been tried by the competing teams. Most of them were of a symmetrical wing with one external flap to alter the shape for lift on either tack [10]. The figures 2.1 below shows four different boats with different wing designs that have been competing. Figure 2.1a shows ‘Hinge’ with a wing that incorporates three independent controlled trailing edge flaps. Figure 2.1b shows ‘Wingmill’ with an asymmetric wing that had an external flap and a leading edge slat. (This boat will be explained in more detail in the next paragraph.) Figure 2.1c shows ‘Edge III’ with a wing that contains a double slotted flap i.e. a wing with two flaps. Figure 2.1d shows ‘Ronstan’ with a wing that incorporates a trailing edge flap and an external flap.



(a) 'Hinge' 1987 [12]



(b) 'Wingmill' 1989 [12]



(c) 'Edge III' 1991 [12]



(d) 'Ronstan' 2004 [12]

Figure 2.1: Four different wingsail designs that have been competing in the *C-Class*

The majority of the boats in the class had symmetrical wings. The American boat 'Wingmill' had an asymmetrical wing mounted on a mast. The wing was attached to the mast at half span; the mast was placed in the centre of the boat with a height of just over half span of the wing (see figure 2.1b). This has the advantage of using an aerofoil profile with less shape compromise i.e. a profile

that is designed to produce lift in one direction. A profile for a low Re (Reynolds Number) range was chosen with a flat stall characteristic [34] in combination with a flap and leading edge high lift device. Inconveniently, the wing needed to be rotated around the mast on every tack and gybe. Unfortunately this boat capsized just before the start line of the 1989 championship. It never finished a race or sailed next to another C-Class catamaran. Due to the testing on the water before the race, the performance of the boat was believed to be at a very high level [34].

Killing emphasises the following points about C-Class catamarans [21]:

- C-Class catamarans are very hard to sail.
- Light simple construction of the wing is crucial, rather than more complex i.e. many flaps, that would result in a heavier wing due to the additional mechanical parts.

If the reader wants to know why hydrofoils are not used in this class, the reader is referred to Appendix C.1.

2.1.2 Wingsail occurrence in other sailing classes

In 1985 and again in 2007 a wingsail made an appearance at the A-Class world championship [38]. The helmsman considered sailing with a wing to be very similar to sailing with a conventional rig, but harder to sail well [38]. In choppy water the boat pitches more due to the higher centre of gravity induced by the mass of the wingsail.

Recently, the prestigious America's Cup saw its first competitor with a wingsail in 2010. The trimaran of *BMW Oracle Racing Team* had a wingsail and also won the cup.

2.1.3 Wingsail research

Two important properties of a wing are the lift coefficient C_l and drag coefficient C_d defined as [39]:

lift coefficient

$$C_l = \frac{L}{\frac{1}{2} \rho V^2 A}, \quad (2.1)$$

drag coefficient

$$C_d = \frac{D}{\frac{1}{2} \rho V^2 A}, \tag{2.2}$$

where V is the freestream velocity, ρ is the freestream density, A is the planform area, L is the lift force and D is the drag force.

The coefficients for a profile section are typically presented in a graph against the angle of attack AoA , such as figure 2.2. A typical lift curve comprise a ‘linear’ region and a curve indicating a drop of C_l with increasing AoA . In the region after the maximum C_l value ($C_{l_{max}}$) the profile section is said to be *stalled*, see figure 2.2. With a flap $C_{l_{max}}$ can be increased as shown in figure 2.2; $AoA(C_{l_{max}})$ will be less than without flap deflection.

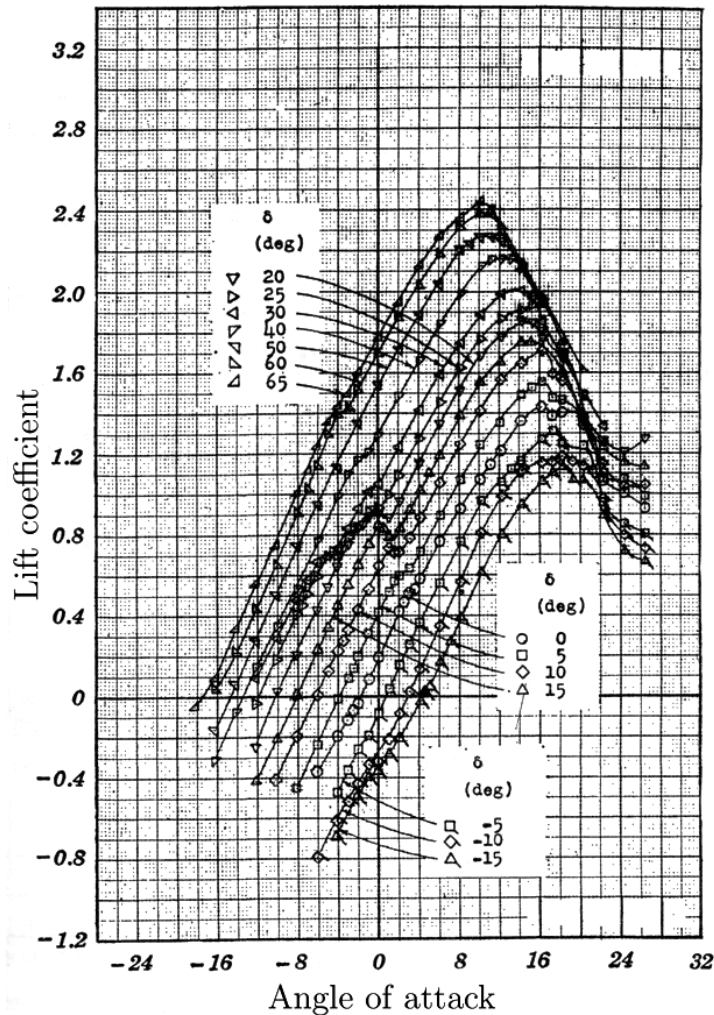


Figure 2.2: Lift polar of a NACA 66(215)-216 profile section with 0.20 chord sealed plain flap with different flap deflections where δ is the angle of the flap deflection; from [4]

The development of wingsails has been driven by sailing enthusiasts, whereas the aerospace industry development of similar profiles is driven by research with significant funding.

The underlying desire to use wingsails in competitive racing lies in their ability to achieve much higher lift coefficients than conventional sails at all points of sail [8].

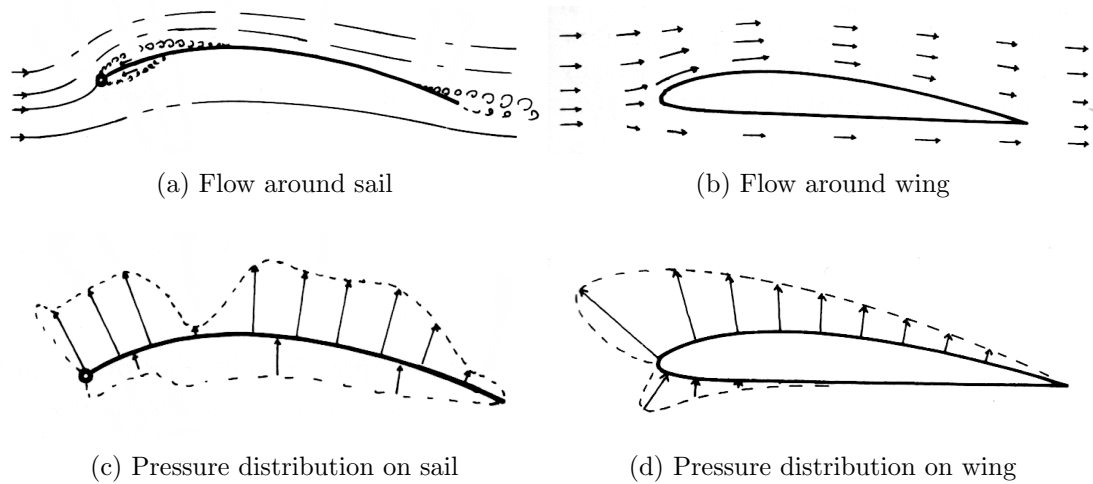


Figure 2.3: Comparison of sail and wing profile; from [8]

The figures above represent the flow around a sail and wing at a low AoA (Angle of Attack). Figures 2.3 show a separation bubble after the mast on the high and low pressure surface. There is also a separation just before the trailing edge on the low pressure surface. This results in different curves of the lift and drag coefficients (C_l and C_d respectively) for a wing and a sail. A sail typically reaches a $C_{l_{max}}$ of about 1.5 and experiences leading stall soon after with sudden significant drop in C_l . Whereas a wing can achieve a $C_{l_{max}}$ of 2 or more [20]. However, in order for a wing to achieve such high lift coefficients, a cambered aerofoil is required. This is the principal problem of wingsails. Since in sailing it is required to sail in both direction relative to the wind, a wingsail needs to have the same properties on both tacks; hence most wingsail designs make use of symmetrical wing profiles. To achieve the same high lift coefficients as cambered aerofoils, symmetrical profiles are assembled as wings with external flaps. With such a configuration high lift coefficients can be achieved by deflecting the flap to either side of the main element.

The early wingsails were the product of sailing enthusiasts with the intention

of reaching the highest performance possible. Those wing designs were based on fundamental wing-theory and experiment. In 1980 a report was published concluding that a tandem design of two drop-nose wing section (see figure 2.4) achieve higher thrust force than the then current *C-Class* catamaran configurations [5].

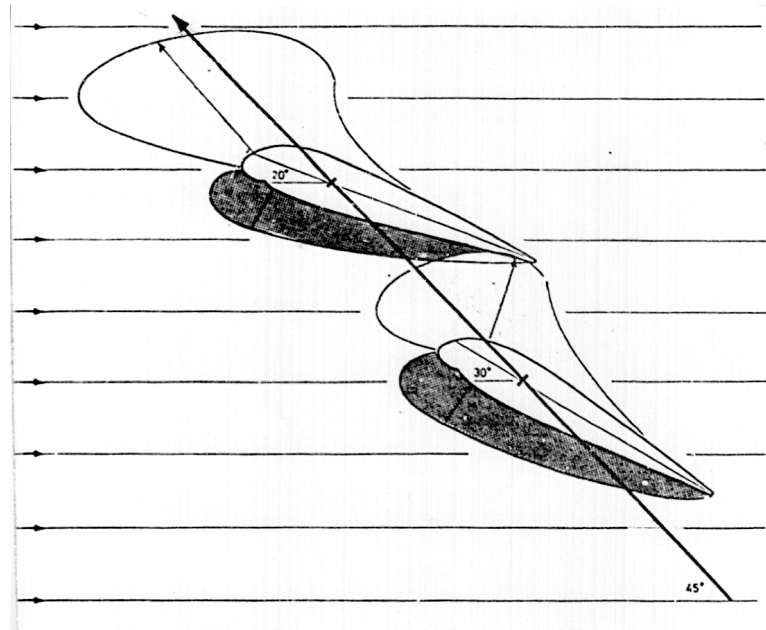


Figure 2.4: tandem drop-nose wing sections; from [5]

In figure 2.4 the horizontal arrows represent the main flow direction. The dark and light areas around the profiles indicate the high and low pressure respectively acting on the profile. That report was based on a wind-tunnel study to find out whether a drop-nose asymmetrical aerofoil is practical. The report also pointed out, that this configuration provides a greater latitude for wingsail adjustment than symmetrical aerofoils or single asymmetrical aerofoils [5].

Research in the field of land-yachts point out another interesting problem. A land-yacht can go very close to wind i.e. the wind is coming from a direction close to the heading; in those situations the camber in a soft sail collapses due to its lack of rigidity i.e. the sail ‘luffs’ in sailing terms [20]. This makes a rigid aerofoil much more efficient at low angles of attack at such courses. Translating this to sailing boat; this gives sailing boats with wingsails a tactical advantage over a boat with conventional soft sail, since it can potentially go closer to wind.

2.2 Physics of sailing

2.2.1 Wind: velocity variations with height

Despite the wide use of SI units the speed in sailing is still measured in knots kts, where

$$1kts = 0.514ms^{-1}. \quad (2.3)$$

When considering the air flow around a sailboat the water needs to be considered as well. The air flow over the water results in a boundary layer flow over the water surface. For a boat this results in a velocity profile where u varies with height.

There are different models to describe the velocity profile. One of them is known as the *log law* typically. The approach summarised in [28] is shown below:

$$u(z) = u(z_r) \frac{\ln \frac{z}{z_0}}{\ln \frac{z_r}{z_0}} \quad (2.4)$$

where z_r is a reference height, z_0 is a surface roughness length and z is the height above the mean water surface. The surface roughness z_0 varies with the waves in different conditions, typical values are given in table 2.1

Surface Description	$z_0[mm]$
Calm open sea	0.20
Blown sea	0.50

Table 2.1: Surface roughness values from [28]

The reference height z_r for a reference velocity u_r is typically 10 meter. Velocity profiles for different values of z_0 are shown in figure 2.5.

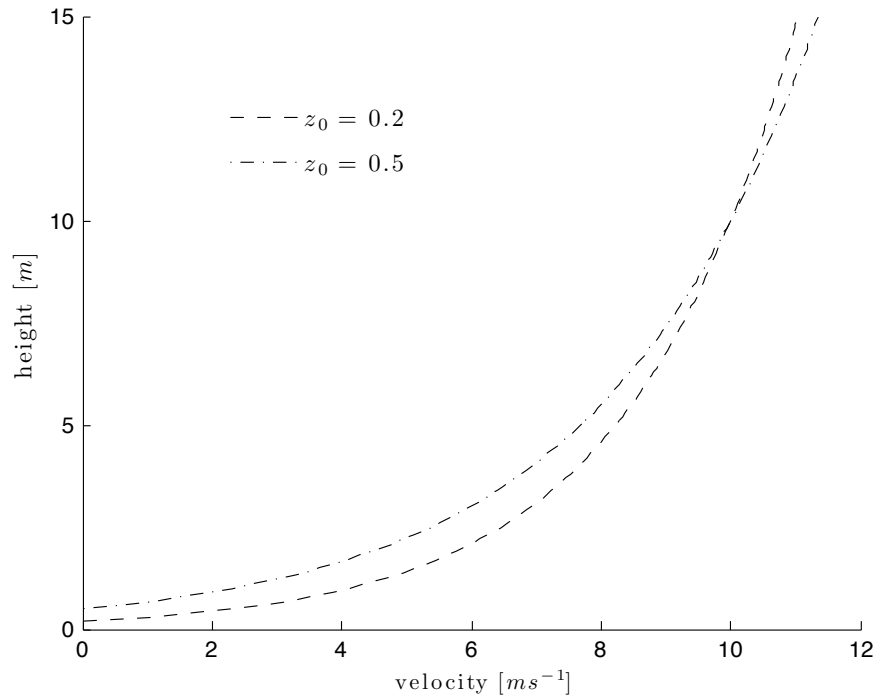


Figure 2.5: Wind velocity gradient with different surface roughness lengths

2.2.2 Apparent wind

At rest the wind direction experienced on a boat is the same direction as the true wind direction. However when the boat is moving the wind direction and intensity experienced on the boat deviates from the true wind direction and velocity. This can be visualised by the use of vectors as shown in figure 2.6.

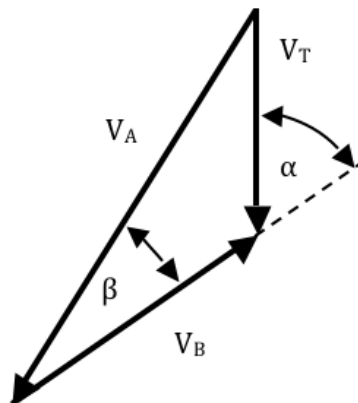


Figure 2.6: Apparent wind speed and direction experienced on a boat

V_T is the true wind, V_B boat velocity and V_A is the apparent wind velocity. From

the figure above, it can be derived that with increasing boat speed the apparent wind not only increases its velocity but also decreases the angle to the heading. If V_T and α stay constant and V_B increases, V_A increases as well and β decreases.

The current C-Class catamarans have boat speeds of 1.5 times the wind speed. This gives a rough estimate for the apparent wind angle β . For upwind sailing β is typically about 20° [34], whereas for downwind sailing β is about 45° [34], see figure 2.7.

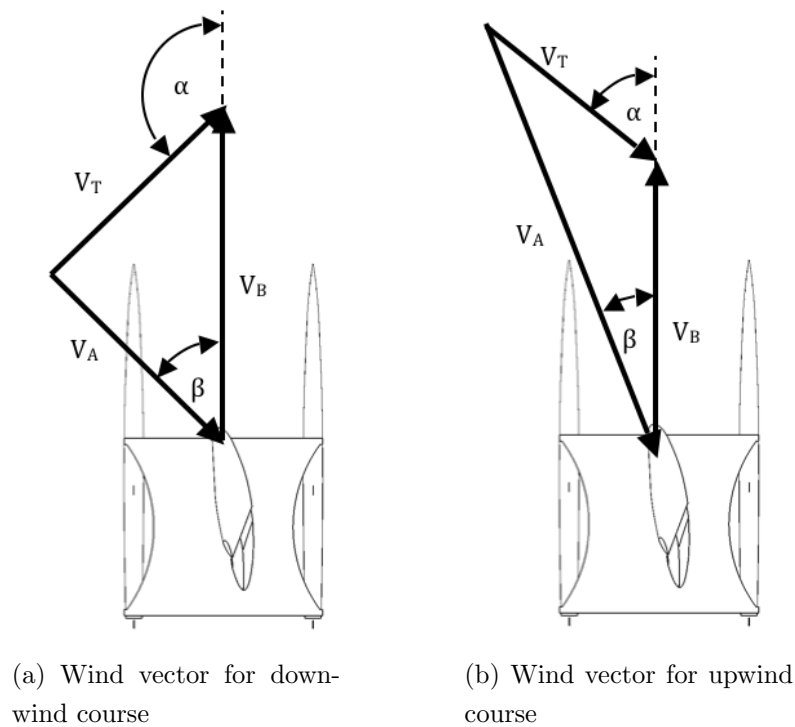


Figure 2.7: Apparent wind typical for C-Class

Wing twist

As the wind speed changes with height, the apparent wind changes with height as well. Thus, close to the water the boat speed and true course has a greater effect on the apparent wind, whereas at the tip of the wing the effect is smaller. This results in a different apparent wind at each finite elevation over the wing.

2.2.3 Righting moment

Multihulls have the potential to reach higher speeds than single hulls [29]. This is due to the righting moment.

On a single-hull boat the water displaced by the hull results in a buoyancy force that is equal to the weight of the boat. The force on the sail is concentrated in the aerodynamic centre and introduces a moment about the centre of buoyancy, causing the boat to heel. This results in a lateral displacement of the centre of gravity in relation to the centre of buoyancy, resulting in the counteracting righting moment to the heeling moment as shown in figure 2.8.

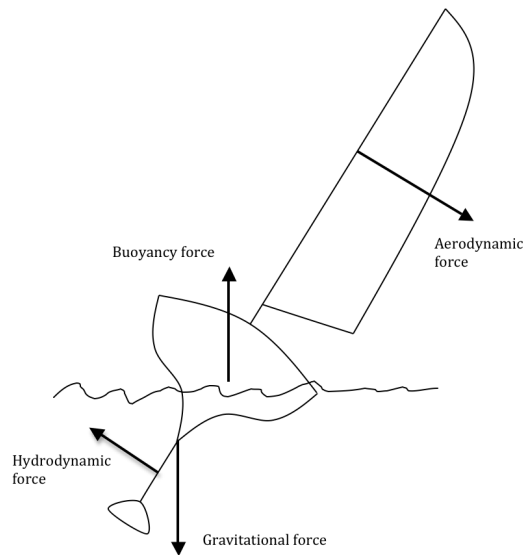


Figure 2.8: Righting moment on a single hull boat

A catamaran works on the principle of having a very high righting moment in steady state. This is achieved by moving the centres of buoyancy and gravity as far apart as possible along the horizontal axis. In sailing conditions, it is desirable to have the leeward hull in the water and the crew trapeze off the windward hull. This generates a high righting moment and thus makes it possible to sail with high sail or wing loads. Thus it is possible to produce higher driving forces (see next section) as for a similar weighted monohull boat.

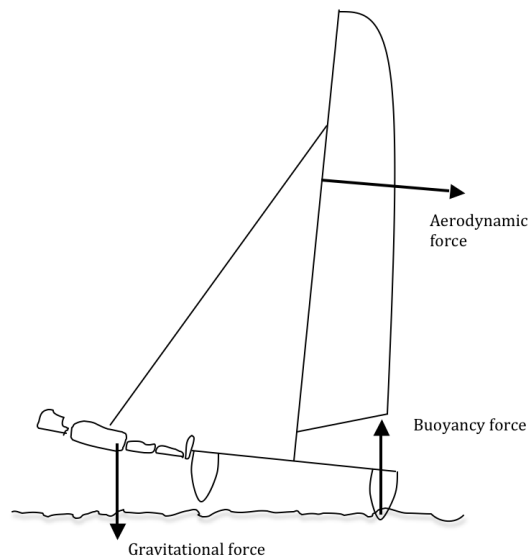


Figure 2.9: Righting moment on a multihull boat

2.2.4 Forces on a boat

The forces generated by the wing i.e. the lift normal to the chord, and the drag axial to the chord translates in to a heeling force or a lateral force and a driving force on the boat, as shown in figure 2.10.

In steady state the hull and dagger board (vertical hydrofoil) produce the same hydrodynamic drag as the driving force in the opposing direction. Similarly, the dagger board of the leeward hull generates the equal amount of lateral force opposing the aerodynamic lateral force shown in figure 2.10. In this state of equilibrium the boat travels in the direction of the heading.

On most dinghies and older yachts, the centre board (or keel) is of symmetrical profile. The yacht drifts naturally during sailing and in so doing generates a small AoA (of the water flow at the centre board). This generates the required force component normal to the chord of the profile. This is a natural process. Subsequently the water flow around the hull is off the ideal flow angle by the drift angle, see figure 2.11. This increases the hydrodynamic drag of the hull.

The idea of modern dagger boards is to use asymmetric profile sections to generate the necessary normal force to produce the required lateral resistant force at zero AoA (of the water flow at the dagger board). This eliminates the drift angle of the yacht.

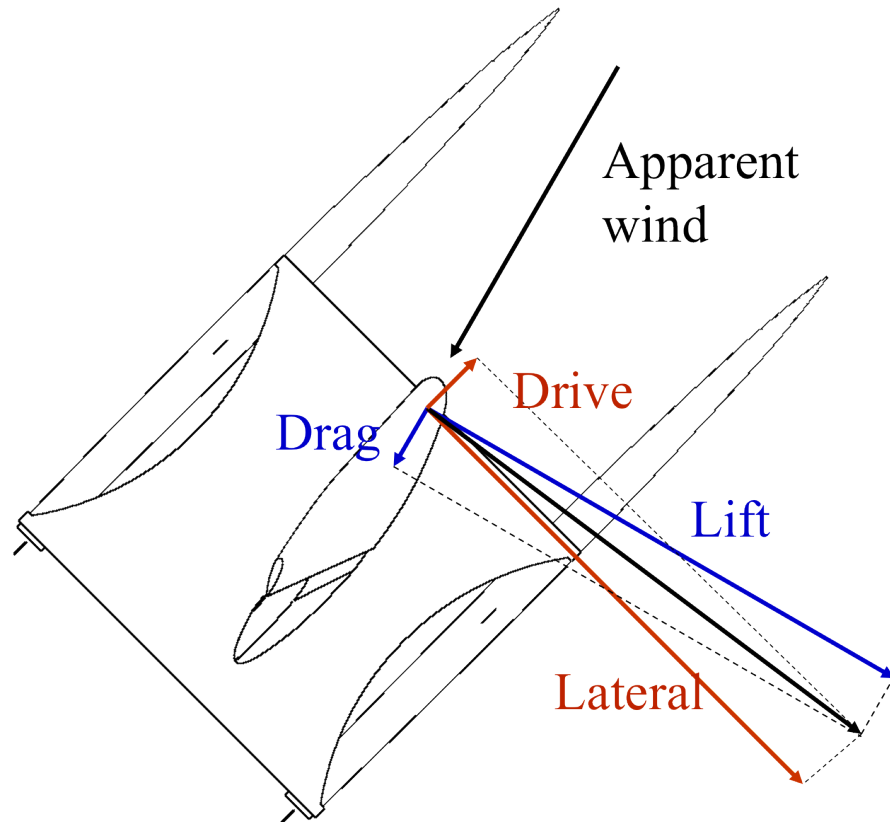


Figure 2.10: Forces acting on a sail boat

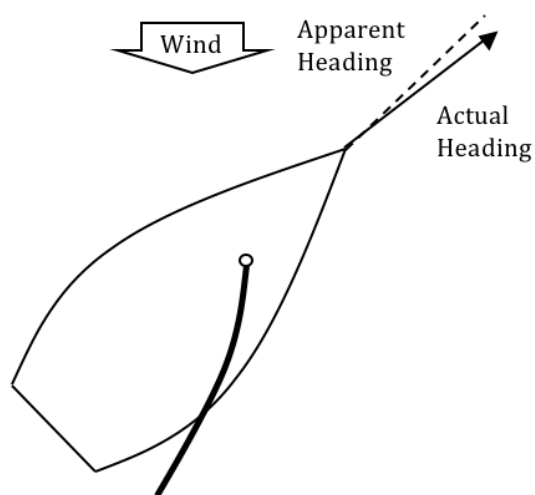


Figure 2.11: Actual heading of a sailing boat with symmetrical centre board

2.2.5 Boat performance requirement for fleet and match racing

Fleet racing

As the name implies a fleet of boats races around a course. The arrangement of the course is highly dependent on its geographic location. Typically, the start is in to the wind and the course comprises of legs of different headings. These courses generally require an all-round good performing boat (upwind, reach and downwind).

Match racing

Match racing is a specific match between two contenders. The course is typically set with a start upwind and a ‘sausage course’ (only two marks that need to be rounded) of an upwind leg and a downwind leg. The course is completed a set number of times before the finish line is crossed. This style of race focuses on the up and downwind performance of the boat.

2.2.6 Sailing upwind

Since it is not possible to sail directly upwind, a very important performance criteria is to go as close to the wind as possible in order to decrease the tacking distance upwind. The fundamental problem of this is that with a constant apparent wind vector an increasing AoA results in an aerodynamic force vector that tends to coincide with the lateral force vector. Recall figure 2.10 for visualisation.

Although having a very low tacking angle is desirable (especially for tactical reasons i.e. making use of rules) it is not the most important property when going up wind. The most important property for a boat sailing up-wind over a race course, is the ‘Velocity Made Good’ to wind (VMG). VMG is defined as the distance travelled to windward in a given time. It is given by the following equation:

$$VMG = V_B \sin \alpha, \quad (2.5)$$

where α is the angle between heading and the true wind and V_B is the boat velocity, as shown in figure 2.12.

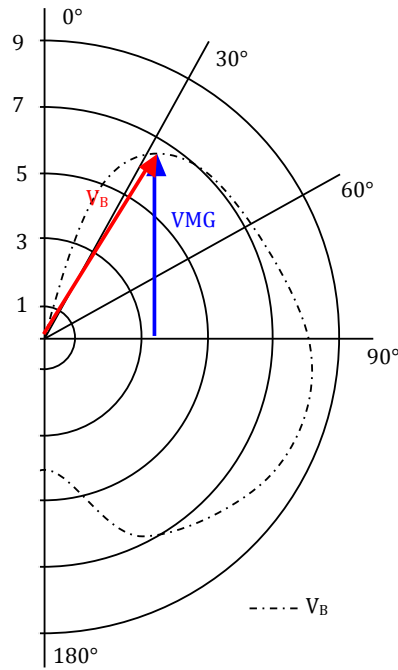


Figure 2.12: VMG for up wind sailing

This figure represents a velocity polar diagram of a sailing boat, where V_B is plotted against the heading to true wind. The red arrow represents the boat velocity vector V_B and the blue arrow represents the actual VMG_{max} vector for sailing up-wind.

The boat velocity polar is required to compute VMG_{max} . This can either be found out by extensive trails on the water (by trying all the possible parameters) or by numerical analysis. The two approaches have different requirements:

- i GPS tracking: This would require to record the true wind, apparent wind and boat speed via GPS. Besides the technical equipment, this would require extensive time on the water in different (and constant) wind conditions.
- ii Velocity prediction: This requires a physically accurate model of the boat to predict the hydrodynamic and aerodynamic forces.

Velocity prediction

A boat is at a constant speed when the forces acting on it reach equilibrium. The apparent wind vector generating those forces on the wing depend on the boat speed, to solve this coupled problem a *velocity prediction programme* (VPP) is

required. In the program, the yacht is accelerated until all forces reach equilibrium with a constant true wind speed and direction. The forces generated by the sail in various configurations can be predicted using *lifting line theory* (LLT) [17]. The LLT bases its lift and drag calculations on 2D aerofoil section data (C_l and C_d). The wing and flap at this point are considered as one. Thus flap deflections are represented as different cambered aerofoil profiles. The aim of the program is simulate it with different sets of parameters to determine the best wing configuration. Consequently, sets of C_l and C_d values for the different flap deflections over a range of $AoAs$ is required.

Flow around the wing

The effect of the flow around the root of the wing is not known [27]. The flow around the hull is believed to have an effect on the lift distribution at the root [20, 35]. However it is uncertain how much the lift distribution is affected. One approach is to assume that the root of the sail is half span [27]. Thus the sail/wing can be modelled as a semi span with a symmetry plane at the root. Scherer argues that if one would make the effort to build a sail that is sealed to the hull (i.e. no gap at the root of the sail), that the effect would not be noticeable. Since this approach has the idea to reduce C_{d_i} (induced drag coefficient; due to wing tip vortex) at the root of the wing, the low wind velocity close to the water surface and the disturbed flow around the hull will diminish that effort [35].

2.2.7 Downwind sailing

As mentioned earlier the procedure for downwind sailing is not to go directly down wind. Higher speeds can be achieved on a broad reaching course. Thus while gybing downwind, higher velocities can be attained.

As mentioned in section 2.2.2 the apparent wind for current C-Class catamarans is typically at about 45° on a downwind course. This changes the requirement for the aerodynamic properties of the wing in this setup compared to the upwind requirements (see section 2.2.6).

An AoA that would make the aerodynamic force vector coincide with the lateral force vector lies beyond stall of the wing profiles currently used. Thus the AoA at $C_{l_{max}}$ defines the maximum attainable aerodynamic force vector in this configuration. However this also results in a very high lateral force (and

increased hull drag) due to the increase of C_{d_i} (induced drag coefficient; due to wing tip vortex) at the dagger board. This is not necessarily the most efficient configuration, hence a VPP is again required to evaluate the best configuration.

2.2.8 Summary of wingsail requirements for a C-Class catamaran

As derived in the previous sections, the general performance requirements for a wingsail are as following:

- High Lift/Drag ratio for upwind performance
- High C_l value at high AoA for down wind performance
- Twist in the chord with elevation to allow for change in apparent wind with height

2.3 Computational Fluid Dynamics (CFD)

The mathematical equations to describe fluid flow are well known. To describe the properties of the fluid, the mass flow, momentum and the energy transport are expressed in three sets of equations known as the Navier-Stokes (NS) equations.

2.3.1 Governing equations

This research is concerned with low speed aerodynamic flow. For flows below Mach 0.3 it can be assumed that the flow is incompressible i.e. constant density [6, 39]. The cases under investigation are assumed to be of attached flows, thus the solution is assumed to be time independent and the time dependency can be neglected in the equations. Also, it is assumed that the effect of gravity can be neglected. The governing equations for the flows analysed in this study comprise:

- Conservation of mass
- Conservation of momentum

The equations required for incompressible and time-independent flows can be written as [39] (Suffix notation will be used throughout):

Continuity equation

$$\frac{\partial u_i}{\partial x_i} = 0, \quad (2.6)$$

where x_i is the space coordinate and u_i is the velocity in the i 'th direction.

Momentum equation

$$u_j \frac{\partial u_i}{\partial x_j} = -\frac{1}{\rho} \frac{\partial p}{\partial x_i} + \frac{1}{\rho} \frac{\partial \tau_{ij}}{\partial x_j}, \quad (2.7)$$

where p is the pressure and τ_{ij} is the viscous stress tensor defined by

$$\tau_{ij} = 2\mu S_{ij},$$

μ is the viscosity and S_{ij} is defined by

$$S_{ij} = \frac{1}{2} \left(\frac{\partial u_i}{\partial x_j} + \frac{\partial u_j}{\partial x_i} \right).$$

2.4 Near wall flows

2.4.1 Flow physics

A flows close to a solid surface comprises a *boundary layer*. The grid in the boundary layer area needs to be adapted to capture the gradients. With increasing Reynolds number the boundary layer reduces in thickness. This results in very fine grids near the wall. Another approach is to use a *wall function* in this area. This only require a much coarser grid but is based on a few assumptions, see section below 2.4.2.

With no-slip conditions the streamwise velocity u is mainly dependent on y (normal to the wall), see Figure 2.13.

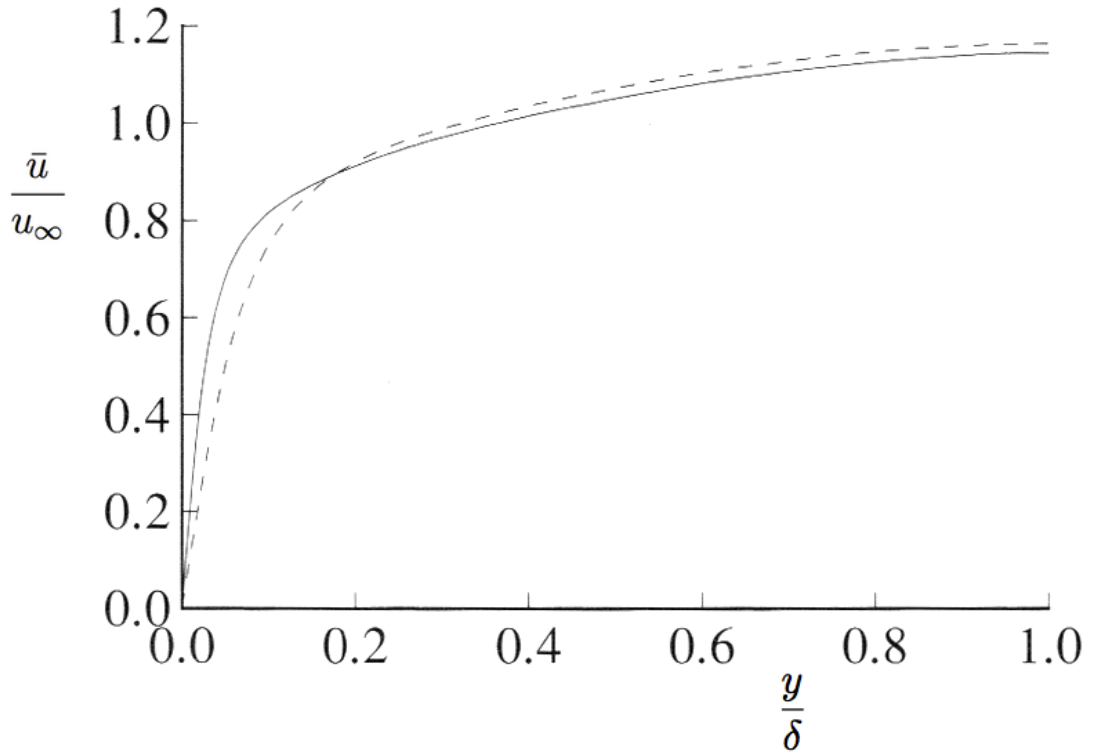


Figure 2.13: DNS data of a channel flow; dashed line, $Re = 5,600$; solid line, $Re = 13,750$, where δ is the centre of the channel; from [32].

Figure 2.13 shows the mean velocity profile of a channel flow.

2.4.2 Modelling of the near wall flows

Wall units

The near wall flow is governed by the shear stresses normal to the flow [32]. The shear stress is the sum of the viscous and Reynolds stresses [32]:

$$\tau = \rho\nu \frac{d\bar{u}}{dx_j} - \rho\overline{u'_i u'_j}$$

DNS data show that the near wall shear stress is dominated by the viscous shear stress, see Figure 2.14. At the wall with a non-slip condition the velocity is zero,

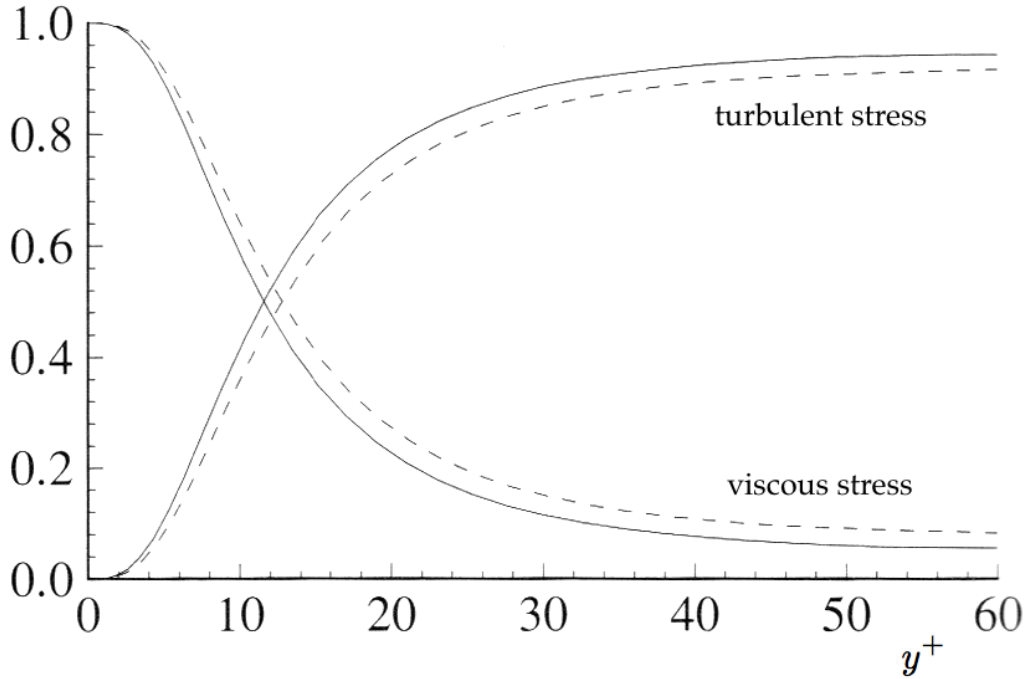


Figure 2.14: DNS data of fractional stress contribution to total stress; dashed lines, $Re = 5,600$; solid lines, $Re = 13,750$ of the flow; from [32].

thus the Reynolds stresses are zero. In the free shear flow the Reynolds stresses are dominant and the viscous shear stresses are neglected. Close to the wall the dominant factor is viscosity. This gives rise to the *viscous scales*. The distance from the wall is measured in wall units [32]:

$$y^+ \equiv \frac{u_t y}{\nu}, \quad (2.8)$$

where u_τ is known as the *frictional velocity* defined by [32]:

$$u_\tau \equiv \sqrt{\frac{\tau_w}{\rho}} \quad (2.9)$$

and τ_w is the shear stress at the wall.

Velocity

Figure 2.15 shows the velocity profile near the wall in viscous units, where u^+ is the velocity in viscous units.

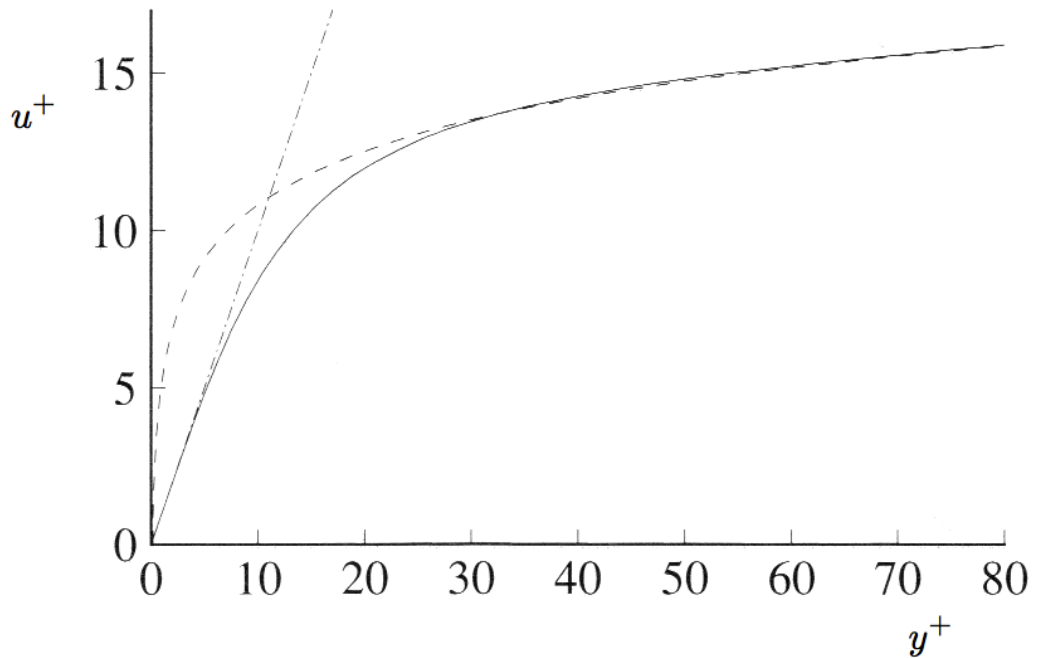


Figure 2.15: DNS data of near wall flow; $Re = 13,750$; dot-dashed line, $u^+ = y^+$; dashed line, the log-law; from [32].

The profile for the log-law region is given by an empirical equation [16]:

$$u^+ = \frac{\bar{u}}{u_\tau} = \frac{1}{\kappa} \ln y^+ + B \quad (2.10)$$

where \bar{u} is the mean velocity parallel to the wall, κ is the von Kármán constant ($\kappa = 0.41$) and B is an empirical constant ($B \approx 5.5$) [16]. The log-law applies in the region $y^+ > 30$. The viscous sub layer dominates the region $y^+ < 5$; in this

region the Reynolds stresses are neglected [32]. The region $5 < y^+ < 30$ is the buffer layer between the viscous sublayer and the log-law region.

Wall treatment

With the wall function approach it is assumed that u , k and ϵ are only dependent on y [16]. It is also assumed that the flow is in local equilibrium, i.e. the turbulent production and dissipation are nearly equal [16].

2.4.3 Grid requirements

Resolving the flow in the boundary layer region requires a very fine mesh of $y^+ < 1$ near the wall to capture the gradients. At high Reynolds number this mesh becomes very fine due to the very small grid spacing in this region. Another approach to compute the flow near the wall is to use a *wall function*. This approach relies on the logarithmic region of the velocity profile [16] and requires a grid size of $y^+ > 30$ at the wall. If the cell size near the wall is < 30 for large portions of the wall boundary, then a low Re model should be used or it must be checked that the code has corrections for use of log-law extensions inside the viscous sublayer (such as scalable wall functions or analytical wall functions). Otherwise this can result in serious modelling errors [16].

2.5 Turbulence modelling

The equations of fluid dynamics (presented in section 2.3) have been known for more than 100 years in their general form [39]. However, solving those equations is a different matter since most engineering flows are of turbulent nature [16]. The characteristic of these flows is that the fluid velocity field varies significantly and irregularly in both position and time [32].

This makes turbulent flows a very computationally intense problem since a very fine grid is required to capture even the smallest variations. Solving the NS equations directly in a domain with a very fine grid; this approach is referred to as DNS (Direct Numerical Simulation). For DNS the NS equations are solved directly for one solution without recourse to modelling. However, the computational power requirement increases (as well as memory requirement) due to the required mesh refinement [32]. Thus DNS is currently (due to limitations of current super computers) unfeasible for high Re (Reynolds number) cases.

One way to explain the requirement for mesh refinement at high Re is with the *Kolmogorov Scales*. The underlying idea is that the kinetic energy enters the turbulence through the large scale motion [32]. The large scale motion drives consecutively smaller scale motions (i.e eddies) during which this energy is transmitted [32]. At the smallest scale the energy is dissipated by viscous action [32].

At high Re flows the characteristic velocity and length scale can be regarded to as Υ and Λ respectively. Thus $Re = \Lambda\Upsilon/\nu$ is large, where ν is the kinematic viscosity ($\nu = \mu/\rho$). The small eddies are of size ℓ and have a characteristic velocity $u(\ell)$ and time scale $\tau(\ell) \equiv \ell/u(\ell)$. Kolmogorov's hypothesis of local isotropy states that the small scale turbulent motion ($\ell \ll \ell_0$ where ℓ_0 is comparable to Λ) at high Re is statistically isotropic [32]. At small scale the dominant parameters are the energy transferred ϵ and viscous dissipation ν . With the two parameters the *Kolmogorov Scales* can be formulated [32]:

$$\eta \equiv (\nu^3/\epsilon)^{1/4}, \quad (2.11)$$

$$u_\eta \equiv (\epsilon\nu)^{1/4}, \quad (2.12)$$

$$\tau_\eta \equiv (\nu/\epsilon)^{1/2}, \quad (2.13)$$

where η , u_η and τ_η are the length, velocity and time scales respectively. With increasing Re the ratio between the smallest and largest scales in the flow is

determined as [32]:

$$\eta/\ell_0 \sim Re^{-3/4}, \quad (2.14)$$

$$u_\eta/u_0 \sim Re^{-1/4}, \quad (2.15)$$

$$\tau_\eta/\tau_0 \sim Re^{-1/2}. \quad (2.16)$$

Thus at high Re , the Kolmogorov scales are very small compared to the large eddies. Hence DNS requires a very fine mesh.

To reduce the computational cost one alternative approach is only to resolve the large eddies and to model the eddies that are smaller than the grid. Such an approach is called LES (Large-Eddy Simulation). However resolving the near wall flow with LES is currently not feasible again due to computational requirements [32]. Thus turbulence modelling is required for near wall flows.

The next step is to fully model the turbulence. This approach relies on predicting the mean velocity and requires an averaged form of the NS equations.

2.5.1 Reynolds Average Navier-Stokes (RANS)

For this approach all unsteadiness is regarded as part of turbulence and is averaged out [16]. Due to the complexity of turbulent flows RANS models should only be considered as engineering approximations of the flow [16]. For turbulent flows the velocity u varies with time and is not known at every instance, see figure 2.16.

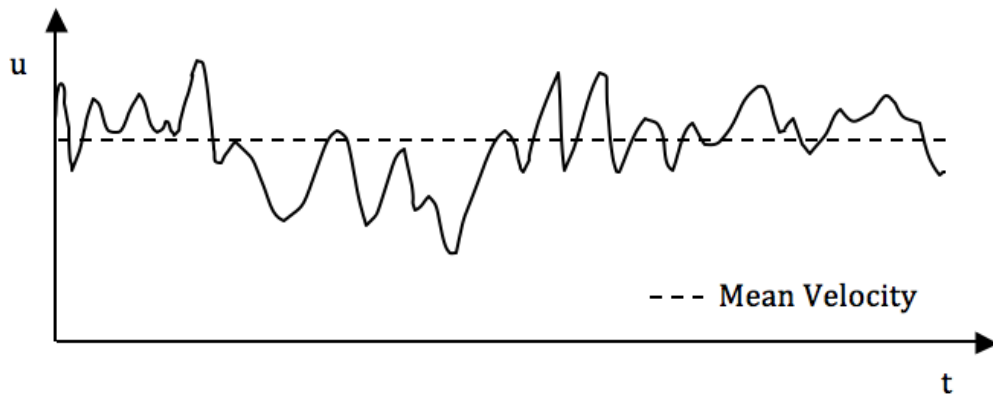


Figure 2.16: Fluctuating velocity about mean velocity

To describe the velocity in turbulent flows, u_i can be decomposed as $u_i =$

$\bar{u}_i + u'_i$. Where \bar{u}_i is the mean velocity and u'_i is the fluctuation (this is known as the *Reynolds decomposition* [32]). Time averaging we obtain the following:

$$\bar{u}_i = \lim_{T \rightarrow \infty} \frac{1}{T} \int_0^T u_i(t) dt, \quad (2.17a)$$

$$\overline{u'_i} = \lim_{T \rightarrow \infty} \frac{1}{T} \int_0^T u'_i(t) dt = 0, \quad (2.17b)$$

$$\overline{u'_i u'_j} \neq 0. \quad (2.17c)$$

Continuity equation (RANS)

Implementing the Reynolds decomposition and time averaging, the continuity equation becomes:

$$\frac{\partial(\bar{u}_i + u'_i)}{\partial x_i} = 0, \quad (2.18)$$

when equation 2.18 is averaged over time, $\overline{u'_i} = 0$ and

$$\frac{\partial \overline{\bar{u}_i}}{\partial x_i} = \frac{\partial \bar{u}_i}{\partial x_i} = 0. \quad (2.19)$$

Momentum equation (RANS)

Due to the convective nonlinear term in equation 2.7, Reynolds averaging applied to this equation yields,

$$\frac{\partial}{\partial x_j} (u_i u_j) = -\frac{1}{\rho} \frac{\partial p}{\partial x_i} + \frac{1}{\rho} \frac{\partial}{\partial x_j} (2\mu S_{ij}) \quad (2.20)$$

and time averaging, we obtain:

$$\frac{\partial}{\partial x_j} (\rho \bar{u}_i \bar{u}_j + \rho \overline{u'_i u'_j}) = -\frac{\partial \bar{p}}{\partial x_i} + \frac{\partial}{\partial x_j} (2\mu \overline{S_{ij}}) \quad (2.21)$$

This time averaged version of the momentum equation includes a new term $\rho \overline{u'_i u'_j}$; it is known as the *Reynolds stresses* [16].

2.5.2 Reynolds stresses

The principal problem of CFD is in determining the Reynolds stresses. This is referred to as the *closure problem*. To close the RANS equations, the turbulent

stresses need to be modelled. One approach is to compute the Reynolds stresses directly.

Reynolds-Stress Models (RSM)

With this approach the Reynolds Stresses and the dissipation are solved directly with model transport equations [32]. RSM require seven turbulence equations to be solved (one for each $\overline{u'_i u'_j}$ and ϵ) [32].

Compared to Eddy-Viscosity models (described in the succeeding section) the RSM can be more accurate for flows with significant mean streamline curvature and swirl [32]. However the required computational work is typically higher [32].

For many flows, practical experience has shown that resolution of the full Reynolds Stress tensor is not required for accurate predictive capability. In these cases, the stress in the flow can be captured implicitly, without recourse to a full transport equation though, for example, eddy viscosity models.

Eddy-Viscosity Models (EVM)

This approach models the stresses via an *eddy viscosity*. This assumes that the turbulent stresses are isotropic. For simple shear flows, the turbulent stress term is rewritten as [32]:

$$\overline{u'_i u'_j} = -\mu_t \frac{\partial \bar{u}_i}{\partial x_j}$$

where μ_t is the eddy viscosity.

Closing the EVM requires an expression for the eddy viscosity. The general approach is to specify the eddy-viscosity as the product of a turbulent velocity v and turbulent length scale ℓ : $\mu_t = v\ell$ [32]. Prandtl proposed to compute the turbulent velocity in terms of the turbulent kinetic energy k [32]. Where k is defined as:

$$k = \frac{1}{2} \overline{u'_i u'_i},$$

thus the eddy viscosity can then be written as [40]:

$$\mu_t = \text{constant} \cdot k^{1/2} \ell.$$

An equation for k can be derived [40]:

$$\rho \bar{u}_j \frac{\partial k}{\partial x_j} = \tau_{ij} \frac{\partial u_i}{\partial x_j} - \rho \epsilon + \frac{\partial}{\partial x_j} \left[\mu \frac{\partial k}{\partial x_j} - \frac{1}{2} \overline{\rho u'_i u'_i u'_j} - \overline{p' u'_j} \right] \quad (2.22)$$

The differential transport equation 2.22 includes terms which are themselves unknown. Hence approximations are required to close this equation [40]. The definition of k includes a quantity, ϵ called the *dissipation* defined by [40]:

$$\epsilon = \nu \frac{\overline{\partial u'_i} \overline{\partial u'_i}}{\partial x_k \partial x_k}$$

Also ℓ is still unknown at this point. The introduction of *two equation models* overcomes this problem since they provide a solution for the length scale. Hence they are known as complete models. There are a number of different approaches in defining the second dependent variable.

2.5.3 The $k - \epsilon$ model

This approach attempts to model the *dissipation rate* ϵ directly. The model was proposed by Jones and Launder [19]. This model is the most popular two equation model [32, 40] and offers the broadest range of applicability (this does not imply accuracy) [32]. Improved coefficients were published by Launder and Sharma [24] with better prediction of the weak and strong shear flow [25]. The original $k - \epsilon$ model in combination with the improved coefficients by Launder and Sharma (as presented below) is referred to as the *standard $k - \epsilon$ model* [40].

Eddy Viscosity

$$\mu_t = \rho C_\mu \frac{k^2}{\epsilon} \quad (2.23)$$

Turbulent Kinetic Energy

$$\rho \frac{\partial k}{\partial t} + \rho U_j \frac{\partial k}{\partial x_j} = \tau_{ij} \frac{\partial U_i}{\partial x_j} - \rho \epsilon + \frac{\partial}{\partial x_j} \left[\left(\mu + \frac{\mu_t}{\sigma_k} \right) \frac{\partial k}{\partial x_j} \right] \quad (2.24)$$

Dissipation Rate

$$\rho \frac{\partial \epsilon}{\partial t} + \rho U_j \frac{\partial \epsilon}{\partial x_j} = C_{\epsilon 1} \frac{\epsilon}{k} \tau_{ij} \frac{\partial U_i}{\partial x_j} - C_{\epsilon 2} \rho \frac{\epsilon^2}{k} + \frac{\partial}{\partial x_j} \left[\left(\mu + \frac{\mu_t}{\sigma_\epsilon} \right) \frac{\partial \epsilon}{\partial x_j} \right] \quad (2.25)$$

Closure Coefficients

$$C_{\epsilon 1} = 1.44, \quad C_{\epsilon 2} = 1.92, \quad C_{\mu} = 0.09, \quad \sigma_k = 1.0, \quad \sigma_{\epsilon} = 1.3 \quad (2.26)$$

2.5.4 The SST $k - \omega$ model

The $k - \omega$ model was the first attempt of a two-equation model, first proposed by Kolmogorov [22]. A new transport equation is introduced to compute the *specific dissipation rate*, ω .

An alternative two-equation model attempts to make use of the strengths of two different two-equation models by combining them. This SST (Shear Stress Transport) $k - \omega$ turbulence model introduced by Menter [31], makes use of a $k - \epsilon$ model transformed in to a $k - \omega$ model and the $k - \omega$ model.

The $k - \epsilon$ model works well for 2D-flows where mean stream curvature and pressure gradient are small [32] and is more robust in free shear flow [40]. The $k - \omega$ model is much superior to the $k - \epsilon$ model in flows with strong adverse pressure gradients [32].

In the SST model the $k - \omega$ model is used in the sublayer and logarithmic part of the boundary layer. Whereas the $k - \epsilon$ model is used in the free flow. Menter also includes a new cross-diffusion term in the ω formulation that has the effect of diffusing ω from the turbulent to non-turbulent region. In this way the solution is unaffected by the free stream value of ω . A blending function is also introduced so that close to walls the $k - \omega$ coefficients are used and far away from the wall $k - \epsilon$ coefficients take effect.

The SST model introduces a modified eddy viscosity function in order to predict flows with strong adverse pressure gradients and predicts pressure induced boundary layer separation more accurately. This leads (for similar accuracy) to higher numerical stability in comparison to the $k - \omega$ model [9].

2.5.5 Choosing a turbulence model

Presented in the previous subsections are the $k - \epsilon$ and the SST $k - \omega$ models. The $k - \epsilon$ is incorporated in many commercial CFD codes and is considered easy and computationally inexpensive to use with wall-functions [32]. However the $k - \epsilon$ performance is poor in boundary layer flows with strong pressure gradients [32].

Turbulence models used for aerodynamics on yacht

The standard $k - \epsilon$ model is shown to be accurate when large parts of the flow is attached [13]. However for flows that are attached for less than large parts, the realisable $k - \epsilon$ model was concluded to be more appropriate [13].

A flow analysis with two-equation RANS turbulence models around a spinaker (separated flow for large parts) was compared to previously conducted wind tunnel tests [23]. The study concluded, that the realisable $k - \epsilon$ model is the best among the tested models. In contrast the standard $k - \epsilon$ and $k - \omega$ models were not very accurate, the SST $k - \omega$, RNG $k - \epsilon$ and Reynolds stress models were not robust [23].

2.6 Finite volume method

For the finite volume method the integral form of the conservation equations are implied [16]:

The equations represented here are for incompressible and time independent flows.

Mass Conservation

$$\int_S \mathbf{u} \cdot \mathbf{n} dS = 0, \quad (2.27)$$

Momentum Conservation

$$\int_S \phi \mathbf{u} \cdot \mathbf{n} dS = \int_S \frac{\Gamma}{\rho} \nabla \phi \cdot \mathbf{n} dS + \int_{\Omega} b d\Omega, \quad (2.28)$$

where Ω is the CV (Control Volume), S is the surface of the CV, \mathbf{n} is the unit vector orthogonal to S , ϕ is the conserved property, Γ is the diffusion coefficient and b are the body forces.

The domain of the case is divided in small control volumes (described in section 2.7). A computational node is placed in the centre of every CV where the variables are to be calculated. Every CV typically shares its faces with adjacent CVs. The surface flux integrals appearing in (say) equation 2.28 are obtained by interpolation between adjacent CV nodes. The solution strategy proceeds by formulating a linear system for the dependent variables at the CV nodes; these are defined by the chosen interpolation method. The linear system is inverted (after boundary conditions are imposed) and the nodal values emerge as the result. To obtain the field values at the computational node, the values are integrated across the faces. In practice, the surface fluxes in equations 2.27 and 2.28 are decomposed into the separate faces making the control volume, i.e. for a (convex) control volume comprising \tilde{k} fields, we have [16]:

$$\int_S f dS = \sum_k^{\tilde{k}} \int_{S_k} f dS, \quad (2.29)$$

where f denotes the term $(\phi \mathbf{u} \cdot \mathbf{n})$ or $(\frac{\Gamma}{\rho} \nabla \phi \cdot \mathbf{n})$ and k denotes the face. As an example, considering a two dimensional discretisation comprising square CVs for simplicity. Then $k = n, e, s, w$ and figure 2.17 shows the arrangement of the CV and its denotations.

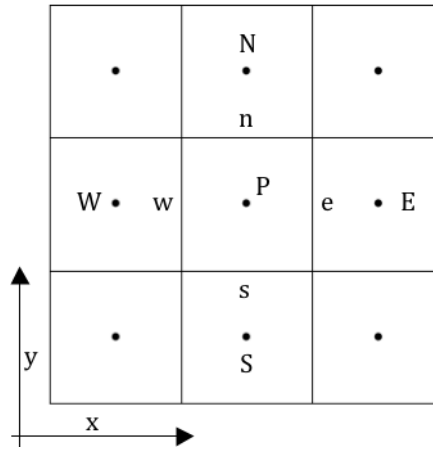


Figure 2.17: CV with the capital letters denoting the computational nodes in the centre and the lower case letters denoting the faces (in respect to P)

If 'e' is considered from figure 2.17, then one would need to know f on S_e . However only the nodal values (at P in this case) of ϕ are known. With the *midpoint rule* the integral can be approximated as a product of the integrand at the face centre and the face area [16]. Interpolation is used to obtain f at the face centre as it is not known [16].

2.6.1 Interpolation

One method is the UDS (Upwind Differencing Scheme). This scheme approximates ϕ_e by the nodal value upstream of 'e' [16], see figure 2.18.

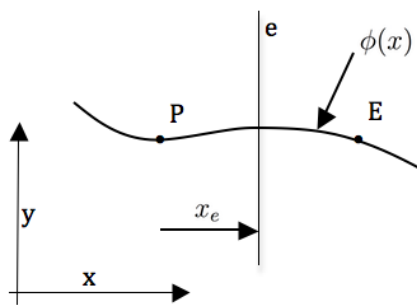


Figure 2.18: Interpolation of the variable

The scheme approximates ϕ_e as [16]:

$$\phi_e = \begin{cases} \phi_P & \text{if } (\mathbf{u} \cdot \mathbf{n})_e > 0; \\ \phi_E & \text{if } (\mathbf{u} \cdot \mathbf{n})_e < 0. \end{cases} \quad (2.30)$$

2.6.2 Discretisation

There are different methods for different orders of accuracy for UDS.

1st-order upwind

For this method (if $(\mathbf{u} \cdot \mathbf{n})_e > 0$) $\phi_e = \phi_P$. By taking the previous known value, oscillations are smeared out. Thus capturing strong gradients requires a very fine grid [16].

2nd-order upwind

For this approach a parabola is defined by the adjacent points, such that [16]:

$$\phi_e = \begin{cases} \phi_P + g_1(\phi_E - \phi_P) + g_2(\phi_P - \phi_W) & \text{if } (\mathbf{u} \cdot \mathbf{n})_e > 0; \\ \phi_E + g_3(\phi_P - \phi_E) + g_4(\phi_E - \phi_{EE}) & \text{if } (\mathbf{u} \cdot \mathbf{n})_e < 0. \end{cases} \quad (2.31)$$

where EE is the node east to E and

$$g_1 = \frac{(x_e - w_P)(x_e - x_W)}{(x_E - x_P)(x_E - x_W)}; \quad g_2 = \frac{(x_e - w_P)(x_E - x_e)}{(x_P - x_W)(x_E - x_W)};$$

$$g_3 = \frac{(x_e - w_E)(x_e - x_{EE})}{(x_P - x_E)(x_P - x_{EE})}; \quad g_4 = \frac{(x_e - w_E)(x_P - x_e)}{(x_E - x_{EE})(x_P - x_{EE})}.$$

2.7 Mesh

In order to compute the flow around a given object, the physical space (domain) surrounding the object must be divided into subdomains via a mesh. The mesh needs to be small enough in locations where there is a change in the flow in order to capture the gradients in the solution.

2.7.1 Aerofoil meshing

Some options available for a mesh around an object are described below [16]. Those options are described in relation to an aerofoil geometry and how they would be applied to it.

- *C-mesh*. A structured mesh that goes around the leading edge and continues downstream beyond the trailing edge. With this mesh, the grid can be refined close to the wing and trailing edge/wake region. The disadvantage of a structured mesh is, that it can only be applied to simple geometries [16]. Also, concentrating the mesh in one region of the domain causes unnecessary small cells in other parts of the domain [16].

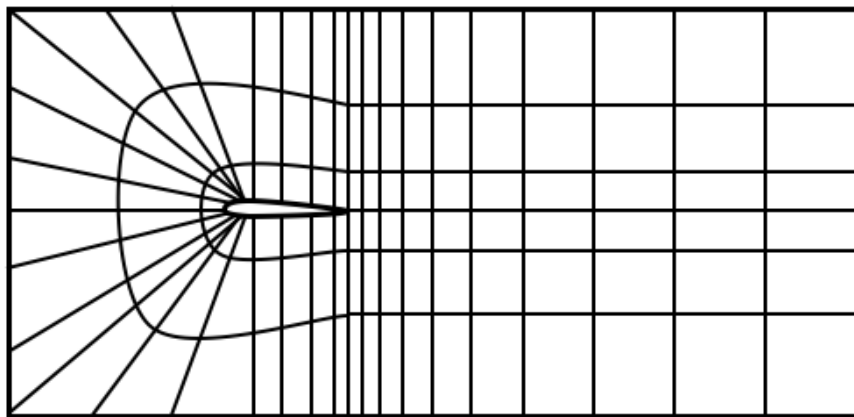


Figure 2.19: General structure of a C-mesh around a single aerofoil

- *O-mesh*. A structured mesh with a circular profile around the aerofoil. This generates a fine structured mesh close to the profile that naturally coarsens away from the aerofoil. However this results in a coarse mesh in the wake region behind the wing.

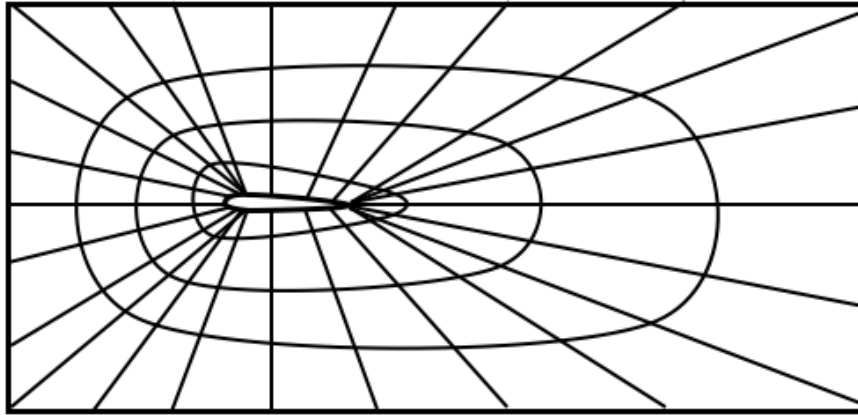


Figure 2.20: General structure of an O-mesh around a single aerofoil

- *Unstructured meshes*; this is the most flexible type of mesh and suitable for complex geometries [16]. For this type of mesh, triangular and quadrilateral elements are used for 2D calculations (tetrahedra and hexahedra in 3D) [16].

Due to the flexibility of unstructured grids they are suitable for complex geometries [16].

2.8 Conclusion of Literature Review

The present research in this field does not suggest one definite turbulence model that is suitable for this case. A comparison of different models is required. Also the decision on the mesh used for this case requires a trade-off between different mesh strategies.

Chapter 3

Methods

3.1 Description of problem

The literature review shows that no significant experimental data is available for this type of application that could have been used in this case study to validate a mesh and a turbulence model. With out experimental data the goal is to build up confidence in the numerical method by minimising the likelihood of error. This will be done by focusing on the following points:

- Mesh refinement studies
- Minimising error due to turbulence model

As the literature review reveals, the application of wingsails is a new research field, without much published research in this field, see section 2.1. This is a very new application of wings, with very little or no sponsored research when compared to the general use of wings in aviation. Reference to wings in competitive sailing only refers to the relative superiority of the aerodynamics of wings over conventional sails [8, 17, 29]. Published scientific work is rare and not current i.e. [5, 7, 35] or only as articles about the sailing experience in high performance sailing magazines [14, 33, 38]. The wingsail only made a recent appearance in the highly sponsored ‘America’s Cup’ in (2010). This cup is widely regarded as the premier event in sailing. Teams in the America’s Cup invest a lot in R&D (Research and Development), however due to the high competitiveness, research is a highly guarded secret [12].

3.2 The wing

The current sailing configuration consists of a wing with a flap. Both wing sections are symmetrical. This is in order to achieve the same properties on a port and starboard course (relative to the wind). The main wing section however consists of two elements; a rigid front section and a flexible trailing edge. Figure 3.1 shows the wing comprises of the main wing section (including the rigid section (blue), the flexible section (green)) and the flap (pink).

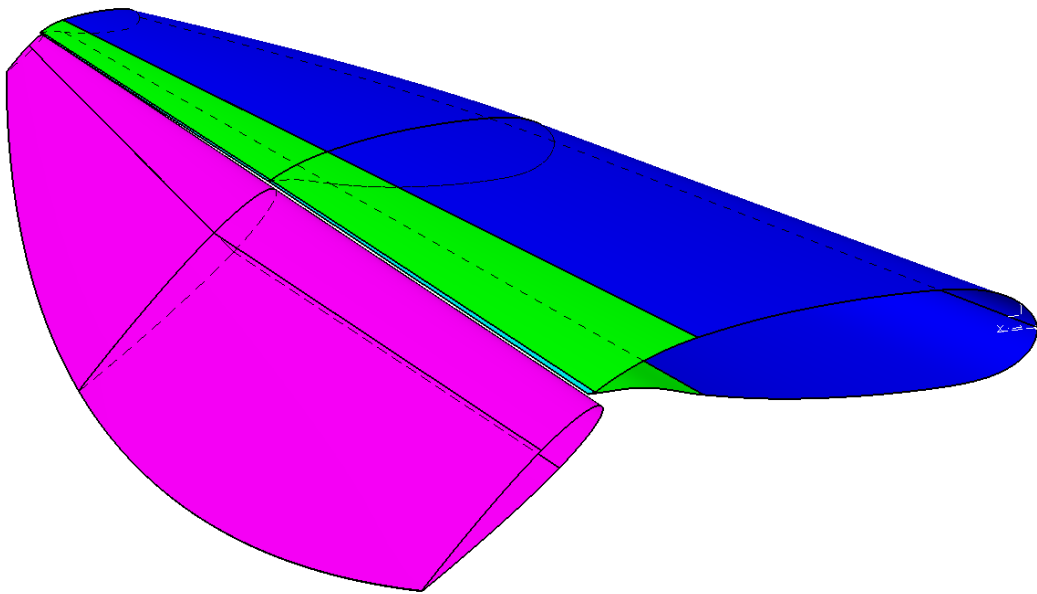


Figure 3.1: Wing and flap profile

The shape of the flexible (green) element is driven by the flap angle. Fingers located on the leading edge of the flap engage the trailing edge of the wing when the flap is deflected, thus controlling the shape of the second element, see figure 3.2. The gap between the trailing edge of the second element and the leading edge of the flap can be adjusted.

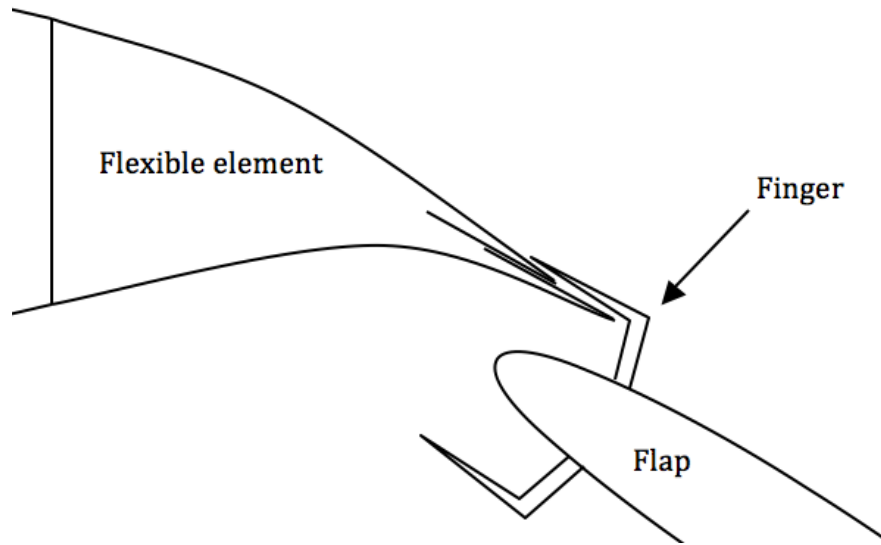


Figure 3.2: Gap control; the two skins are not attached to the each other at the trailing edge and slide along each other when morphed.

When deflecting the flap, it is only the skin of the flexible element that is morphed. The flexible element comprises of a thin skin that is extended as a straight sheet off the rigid section. The skin in this area is made of a few layers of carbon fibre and deflects under the load imposed by the fingers.

The profile of the main wing section (see figure 3.3) is reverse engineered by Team Invictus from a previous successful catamaran ‘Alpha’. The idea behind the large rounded leading edge is to suppress early stall [4]. The morphing element is a modification made by Team Invictus to the design of Alpha’s wing. The flap itself has a NACA 0010 profile.



Figure 3.3: Aerofoil section of main wing (trailing edge not deflected)

The spanwise shape of the wing is made of those two profiles, both of which are scaled according to the span-wise location and required chord length. This wing configuration has a average chord ratio (wing/flap) of about 46%, see figure 3.4 the spanwise shape.

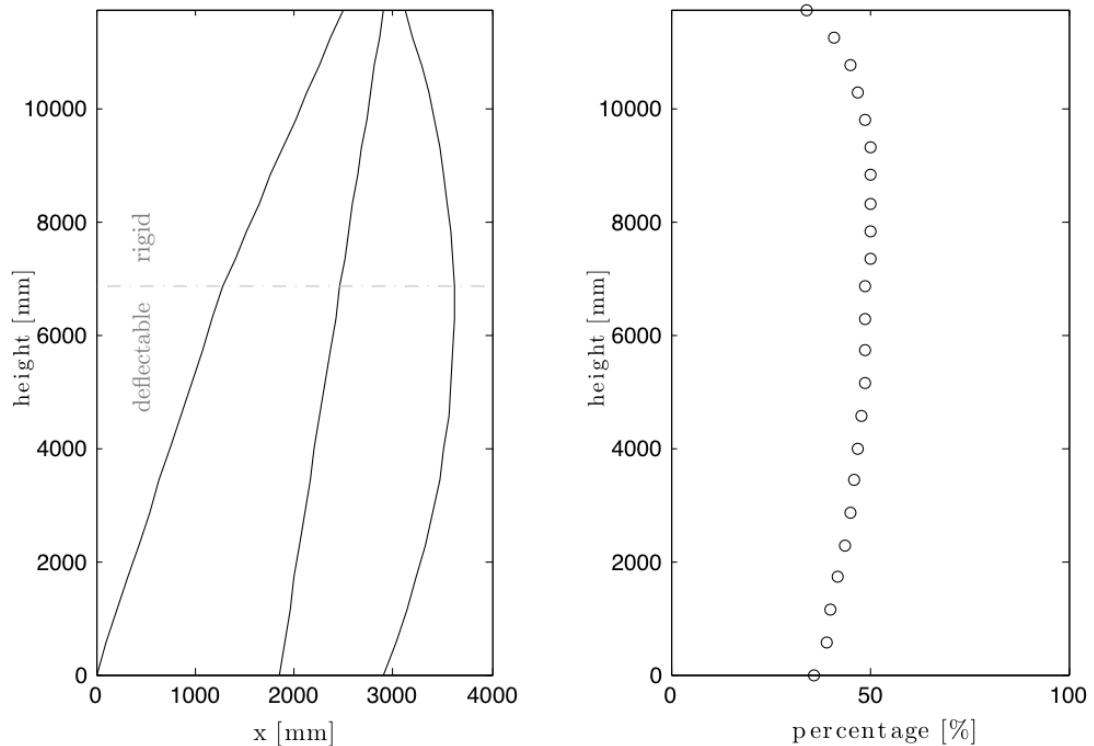


Figure 3.4: The graph on the left shows the planform of the wing. The right graph shows the flap chord percentage to the overall chord.

To compensate for the change in apparent wind due to height, the wing can be partially twisted. The span of the wing is 11.75 m. The top section of the wing from the point of the shroud attachment (at 6.86m) is not twistable. The section from the lower wing tip to the shroud can be twisted linearly.

3.2.1 Wing setup and use

The wing is currently (at time of writing) subjected to trials on the water. The gap between flap and trailing edge of the flexible element for this wing is currently set to a constant 3% along the span. Measured relative to the chord of the main wing. On upwind runs the flap was found to be efficient at a deflection of 15° . On broad reach courses the flap was deflected to about 40° s. The way the wing was manufactured allows a maximum flap deflection of 45° .

3.3 Modelling requirements

From a pure practical sailing point of view there are two major performance points:

- Maximum C_l/C_d for maximum thrust on upwind courses
- $C_{l_{max}}$ at high angles of attack for maximum thrust at broad reach courses i.e. down wind courses.

C_l and C_d polars are required as inputs in to a VVP (Velocity Prediction Program). For this application polars cover the AoA range of the linear C_l region. Due to the change in apparent wind, maximum C_l/C_d and $C_{l_{max}}$ is not enough on its own, as described in section 2.2.6. Thus,

- A range of configurations (different flap deflections) is required to cover the above mentioned performance requirements.
- Polars are required for those configurations.

Another requirement is to investigate the influence of the gap between the two profiles i.e. the effect of different gap sizes on the C_l and C_d polars. Thus,

- the polars need to be obtained for different gap sizes.

From a pure VPP point of view, the modelling of the wingsail root is not well defined, as described in section 2.2.6. It is uncertain if or how the water surface and the hull of the boat affects the root tip vortex and the general flow around the wing. Thus it is required to identify:

- If the water surface and hull affects the root vortex and thus flow around the wing.

3.3.1 Tackling the modelling requirements

The modelling requirements can be categorised in to two problems in terms of modelling:

- 2D simulations for the polars
- 3D simulations for the large scale flow around the wing.

The following sections describe the mesh generation and setup of the 2D and 3D cases.

3.4 2D mesh generation

Since the convergence and accuracy of the simulations are highly dependent on the mesh, great care is required in choosing a mesh approach that accommodates all the above requirements. The unstructured mesh approach was taken. The problems associated with a structured mesh around the geometry under investigation are given in Appendix D.

Unstructured mesh

In an attempt to generate a mesh that provides a reasonable cell quality in the gap and far field region, an unstructured mesh (triangles) with prism layers in the boundary layer was used.

The area of structured mesh (prism layers) was defined by a constant distance around the profile. The distance was defined as a percentage of the distance between trailing and leading edge in the gap (see figure 3.5(c)). This provided a similar distance between the two prism layer regions in the gap. This ensured that the mesh in the gap was very similar among cases with different gap sizes.

The domain was defined as a circle. In order to control the cell size in the far field and in the wing region, geometrical circles were introduced to define areas for mesh refinement. The diagrams in figure 3.5 show the geometry that was used to guide the mesh generation.

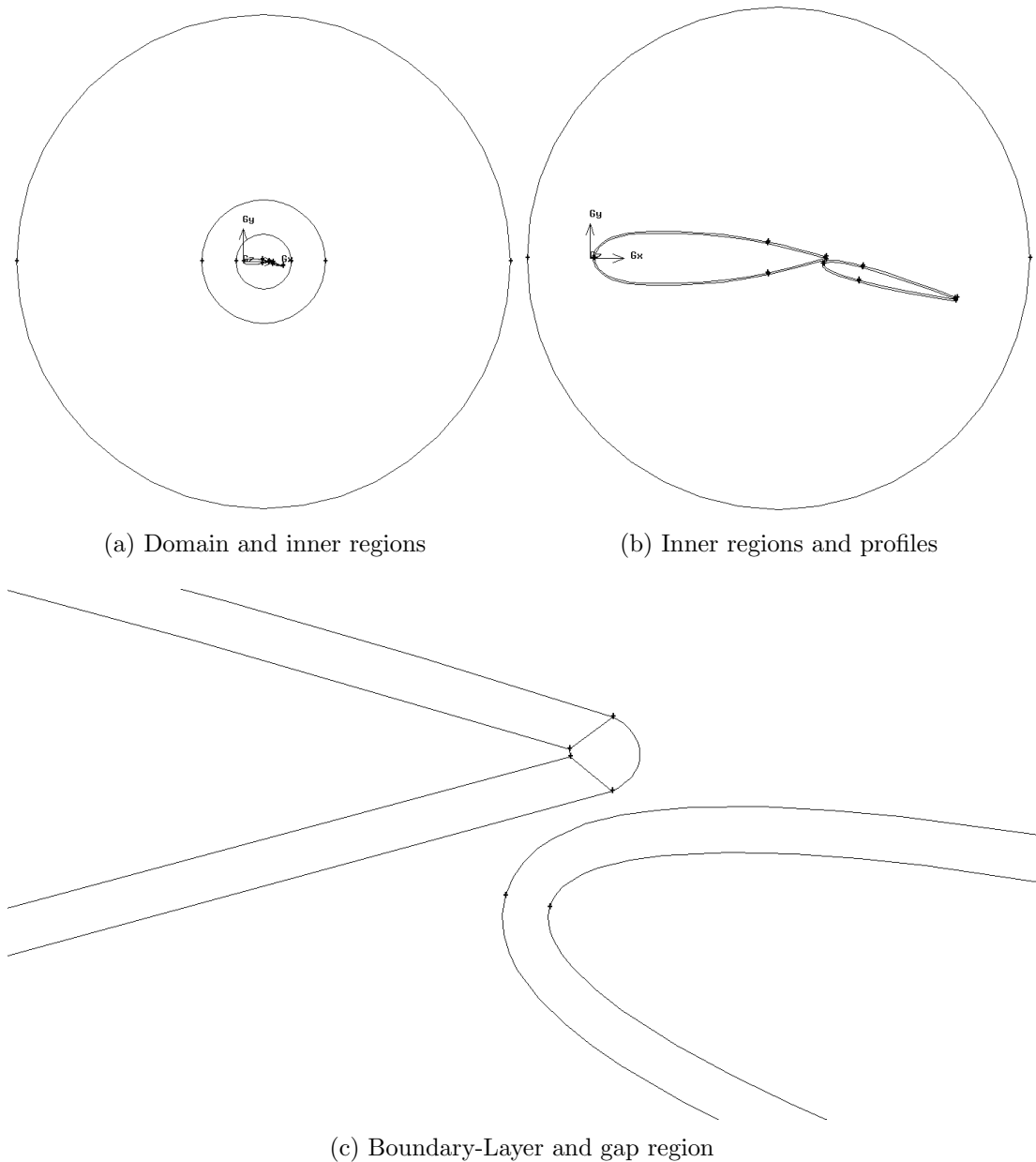


Figure 3.5: Geometry to guide the mesh generation. These figures show the profiles in a configuration with a gap of 2% and a flap deflection of 15° .

Without wind tunnel data for this aerofoil available, C_l and C_d values produced by the simulations could not be compared to experimental data. Although there is a rich literature in the field of wing-flap configurations there are two differences to the design under investigation when compared with aerospace applications:

- i The geometry is very different. Aeroplanes use a slotted flap design (double

or triple slotted on common single and double aisle planes) in contrast to an external aerofoil flap design. The retractable flap design in the former improves the maximum lift coefficient without changing the characteristics for cruising and high-speed flight conditions [4].

- ii The optimum Re (Reynolds number) range encountered during flight is different from those studied here.

To compare the solution of the mesh to a low Re wind tunnel test, experimental data from a NACA 0012 was taken. While this does not reproduce the stall characteristics of a multi element aerofoil; at low AoA in the linear C_l region the flow characteristics should be simple enough for solution comparisons (i.e. flow is attached over the entire profile).

The mesh around the NACA 0012 was generated in exactly the same way as for the multi element wingsail. With this configuration a mesh refinement study could be undertaken. Grid independency of the solution could be established and thereby establishing the credibility of the approach adopted (see Appendix E for the results).

After mesh refinement studies, the final mesh for the multi element aerofoil was as shown in figure 3.6:

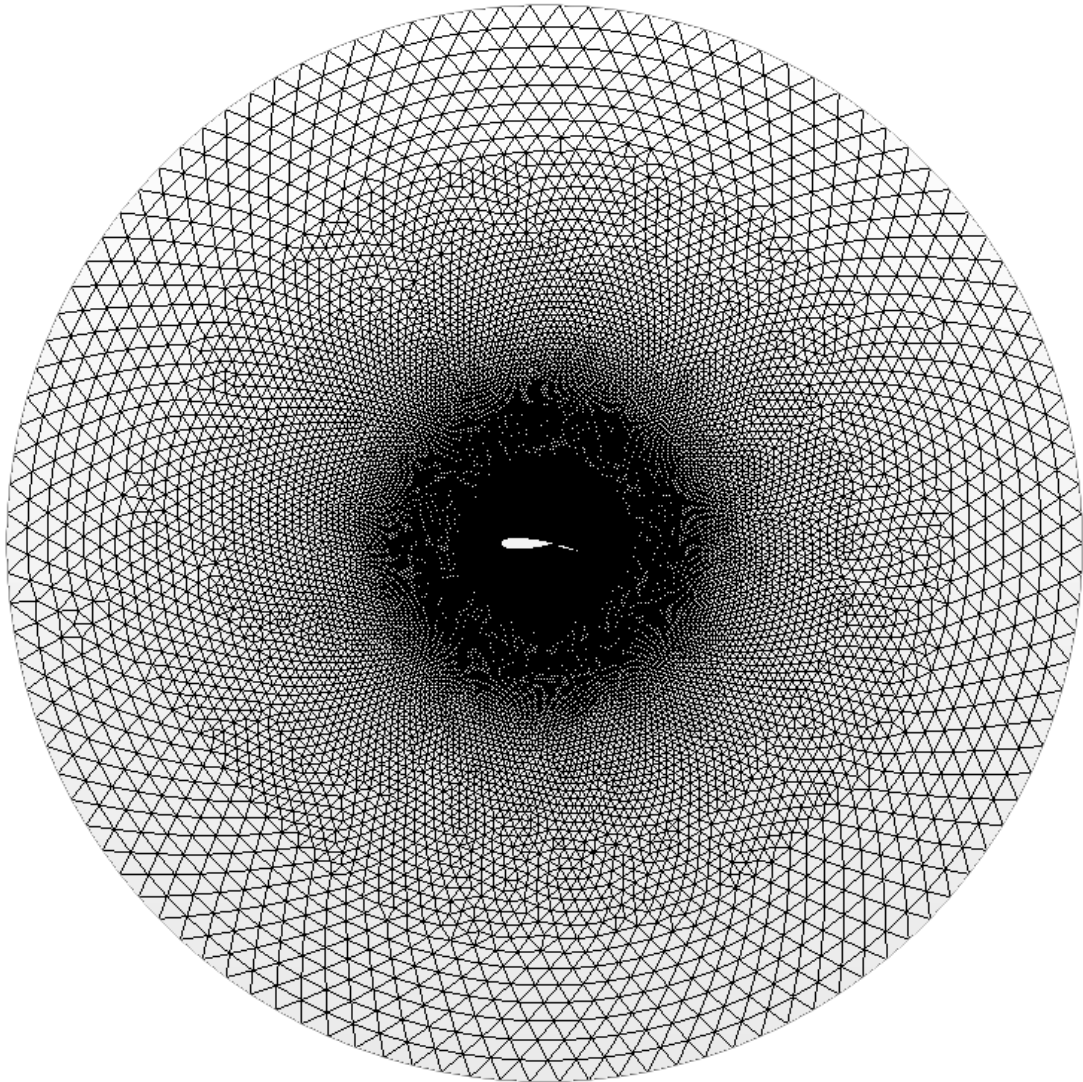
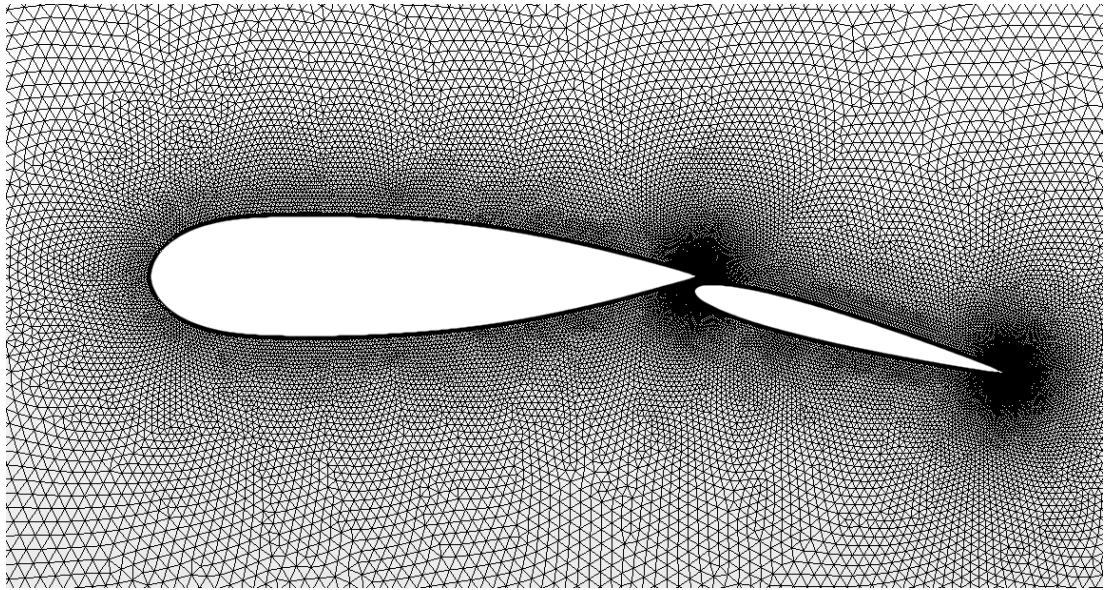
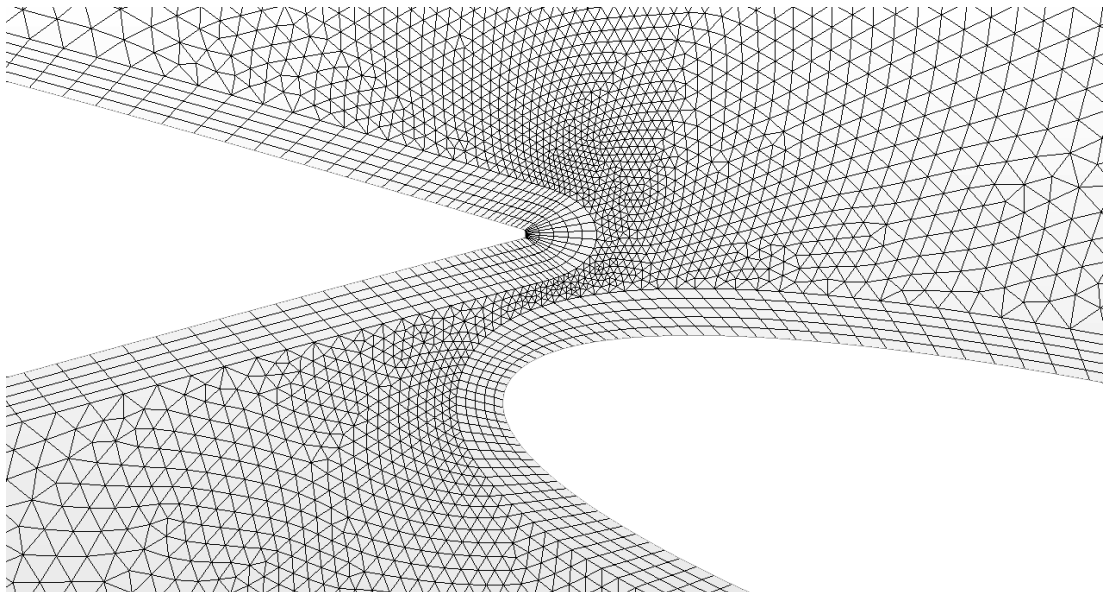


Figure 3.6: Domain and inner regions

The mesh immediately around the airfoil is fine and coarsens out towards the far field. Around the profiles the mesh was kept in the y^+ range described below.



(a) Inner regions and profiles



(b) Boundary-Layer and gap region

Figure 3.7: Mesh around the profiles. These figures show the profiles in a configuration with a gap of 2% and a flap deflection of 15° .

The y^+ values near the wall vary along the profile. The first layer of the prism cells near the wall has a constant height. Thus the cell height should lie within the effective y^+ range in order to ensure good results for the standard wall function used here. As described in section 2.4, the guideline for the y^+ range is $30 < y^+ < 300$. With flows from velocities $V = 0$ (at the stagnation point) till

$V \approx 16$ accommodating this range is impossible on a constant layer thickness. Thus care was taken where the range is exceeded. The first cell layer height was tailored so that the y^+ was within the prescribed range at the leading edge and on the suction side of the aerofoils. The y^+ along the profile of the two aerofoils is given in figure 3.8.

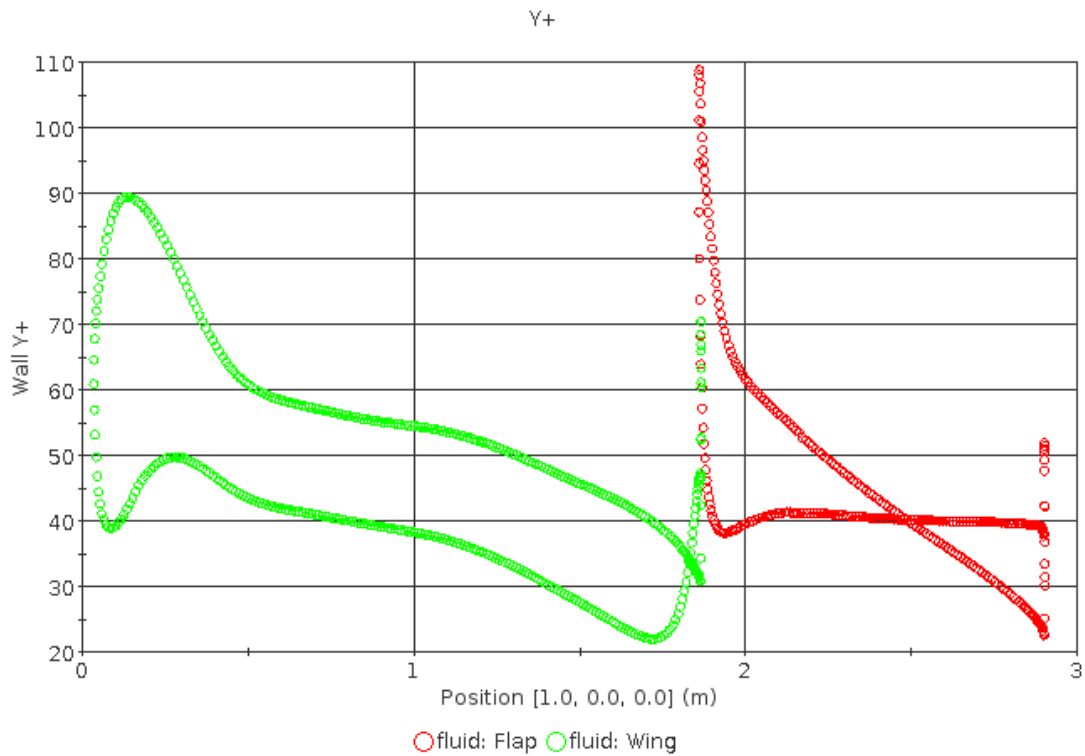


Figure 3.8: y^+ range for the two profiles with a gap of 2% and a flap deflection of 15 degrees

3.5 2D simulation setup

3.5.1 Considerations

Commensurate with the conditions the fleet and match races are held in, it was assumed that the conditions of the standard atmosphere at sea level apply. The values are as following:

Properties	values
Pressure [N/m^2]	$1.01330 \cdot 10^5$
Density [kg/m^3]	1.225
Dynamic Viscosity [$N \cdot s/m^2$]	$1.7894 \cdot 10^{-5}$

Table 3.1: Relevant properties of air at sea level and 15°C for the standard atmosphere.

On the water the intensity and direction of the wind varies over time. In this study, only the steady wingsail response is of interest, not how the boat is handled by the sailor. Thus the flow conditions are assumed to be constant for this purpose.

The boats in this class are built for true wind speeds of up to 20 [kts] (see section 2.1.1), thus the flow can be assumed to be incompressible [6].

The nature of the wind experienced by yachts is of turbulent nature due to the turbulence in the earth's boundary layer flow [15]. The non-dimensional *Reynolds number* Re describes the state of the flow, defined as [39]:

$$Re = \frac{\rho VL}{\mu} = \frac{VL}{\nu}, \quad (3.1)$$

where V and L are the characteristic velocity and length scales respectively. ρ is the density, μ is the dynamic viscosity and ν is the kinematic viscosity defined as [39]:

$$\nu = \frac{\mu}{\rho}. \quad (3.2)$$

The transition from laminar to turbulent flow is given as $Re_{tr} \approx 5 \times 10^5$ [39]. According to equation 3.2 with the environmental condition stated above the transitions to a turbulent boundary layer flow appears after:

$$\frac{5 \times 10^5 \times 1.7894 \times 10^{-5} [N \cdot s/m^2]}{1.225 [kg/m^3] \times 10 [m/s]} \approx 0.73m \quad (3.3)$$

Since the chord of the wing exceeds this distance the flow can be assumed to be turbulent.

The time limit of the project precluded a turbulence model comparison among the RANS models that are available. As described in section 2.5.5 the $k - \epsilon$ model has proven to be robust for different flows encountered in sailing but under predicts separation [13, 23], while the *SST* was shown to be not very robust [23].

The test case presented in Appendix E shows that $k - \epsilon$ is sufficient for predicting C_l and C_d in the ‘linear’ C_l range. The *SST* model was slightly superior in the prediction of C_l and C_d . However this model was not very robust for flows around the multi element aerofoil with the meshes generated. The *SST* model provided to be difficult to converge.

For the simulation setup see Appendix F.

3.6 3D Mesh Generation

The mesh approach (cell sizes and growth rates) used for the 2D profiles cases was not applicable for this mesh, since it would create a mesh that would have been too big for the resources and time available for this project. The general goal was to generate a mesh that has a cell count of roughly less than 5 million cells.

The aim was to visualise the flow around the wing and the forces acting on the wing. In order to obtain the difference between the flow only around the wing and around the wing with the boat and water two simulations are required. Thus two meshes were generated, presented in the following two sections. The mesh described below is for a wing with a flap deflected at 15° . The model including the boat is a setup where the wing is rotated 15° to starboard with a flap deflection towards the centre of the boat of 15° . This is an up-wind configuration of the boat. Due to the lack of VPP data at this point, the setting is an estimate of the boat setup for an upwind course.

3.6.1 Wing Mesh

The geometry of the model was not refined for this purpose; it was provided as a CAD model (Computer-Aided Design). The only adjustment made to the wing was the gap. As described previously, the gap is set as a percentage of the main chord, thus it is very small at the tip of the wing. In order to satisfy the minimum resolution requirement of $y^+ > 30$ the gap was set to a constant distance over the entire span. The distance for the 2% gap was applied over the entire span, thus a boundary layer mesh was applied to the entire wing. With the general aim to generate a small mesh, the difficulty was to maintain a representable shape of the wing at the leading edge, especially the leading edge of the flap and the gap region when applying a coarse mesh.

The general mesh approach was smaller cells at the leading and trailing edges with coarser mesh mid chord. The volume mesh was defined by a pre-specified growth rate in cell size towards a maximum value of 6m. This ensured a relatively fine mesh in the near wing field with a coarse mesh in the far field. During the mesh generation process it was found that a fine mesh in the gap region was crucial. A coarse mesh in the gap region affected the convergence in a negative way i.e. the simulations with a coarse mesh in the gap region did not converge.

The final mesh of the wing in the domain had about 7 million cells. The domain was set to an elliptical extrusion around the wing, placing the wing in the upstream part of the ellipse, as shown in figure 3.9. The mesh refinement around the wing is shown in figures 3.10 and 3.11.

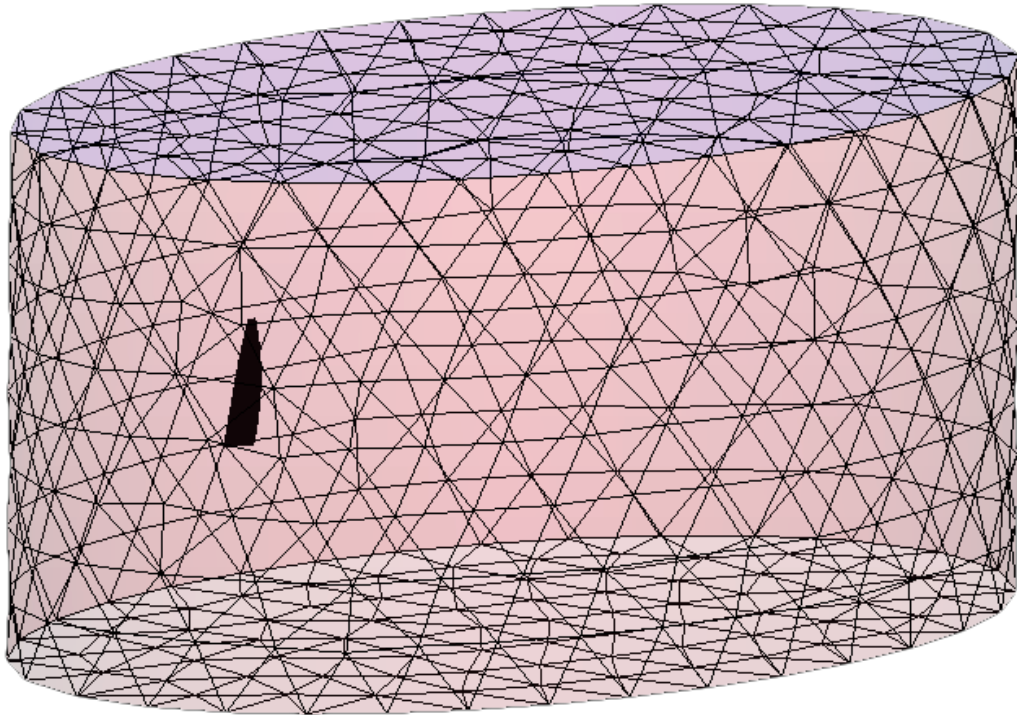


Figure 3.9: The domain and the wing mesh



Figure 3.10: The wing mesh

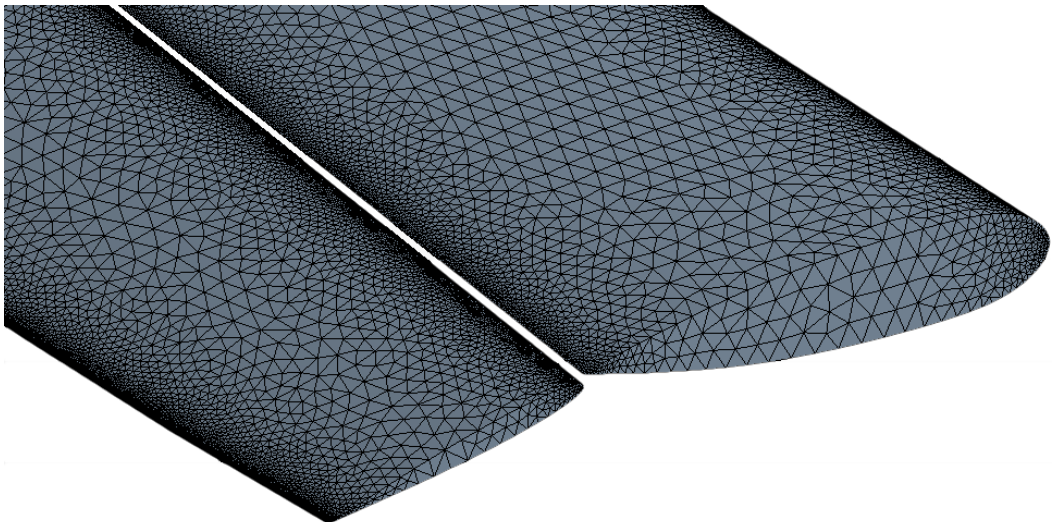


Figure 3.11: The wing mesh

3.6.2 Wing with Boat Mesh

During the mesh generation process many meshes were tried, ranging from 3 million to 25 million cells. The final mesh had a cell count of 14 million. The domain is of elliptical shape, where the water surface is the bottom flat face, as shown in figure 3.12. The mesh refinement around the boat and the wing is shown in figures 3.13 and 3.14. The mesh of the wing was the same as for the case described previously. The mesh around the two hulls and the trampoline was refined towards the corners with the same values as at the wing.

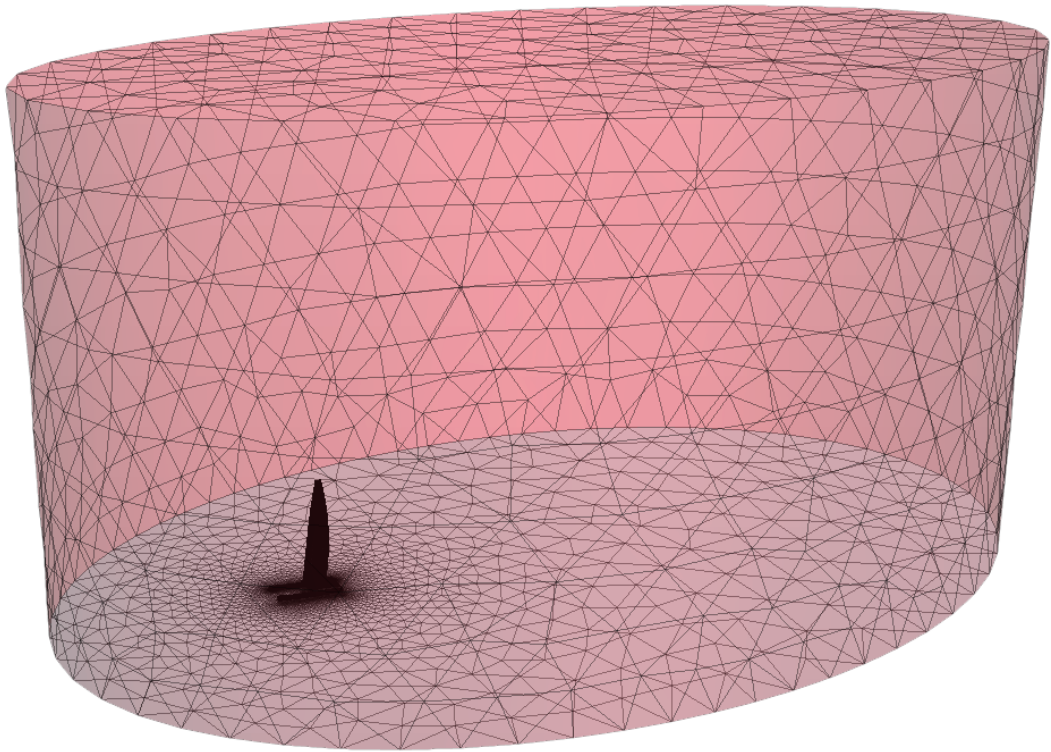


Figure 3.12: The domain and the wing mesh

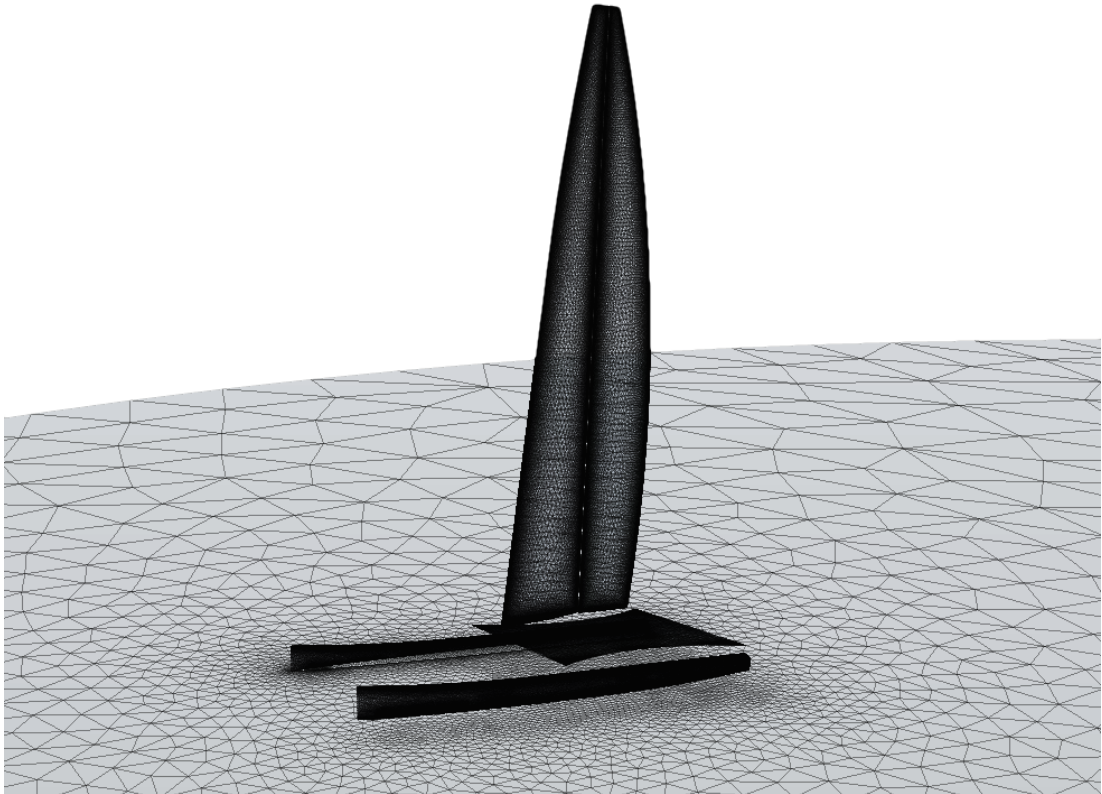


Figure 3.13: The hulls and wing mesh

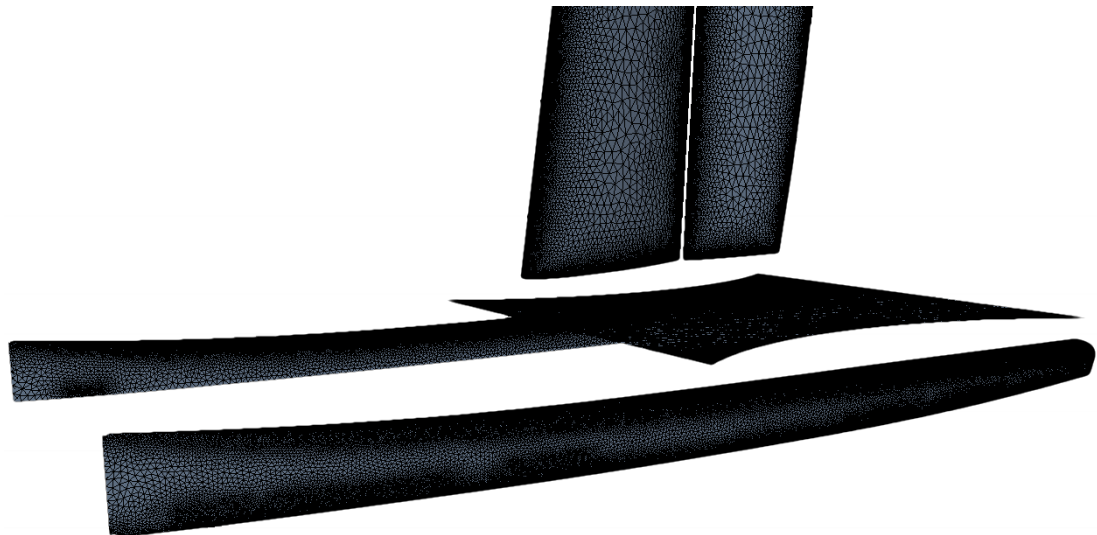


Figure 3.14: The hulls and wing mesh

3.7 3D Simulation Setup

The 3D simulations were setup in the same way as the 2D simulations in terms of the mathematical modelling, see section 3.5. The discretisation for mass and momentum was set to first-order upwind.

The case under investigation was an upwind configuration. Due to unfortunate circumstances ‘Team Invictus’ was not able to supply VPP data with the exact apparent wind and wing setup for this condition. Thus assumptions regarding those values were made.

For the purpose of this investigation the following assumptions were made:

- Apparent wind angle of 20° to heading.
- Flap deflection of 15° .
- AoA of 5° (relative to main wing chord).

For the initial investigation the velocity profile of the wind was ignored. A constant velocity across the domain was assumed, as shown in figure 3.15

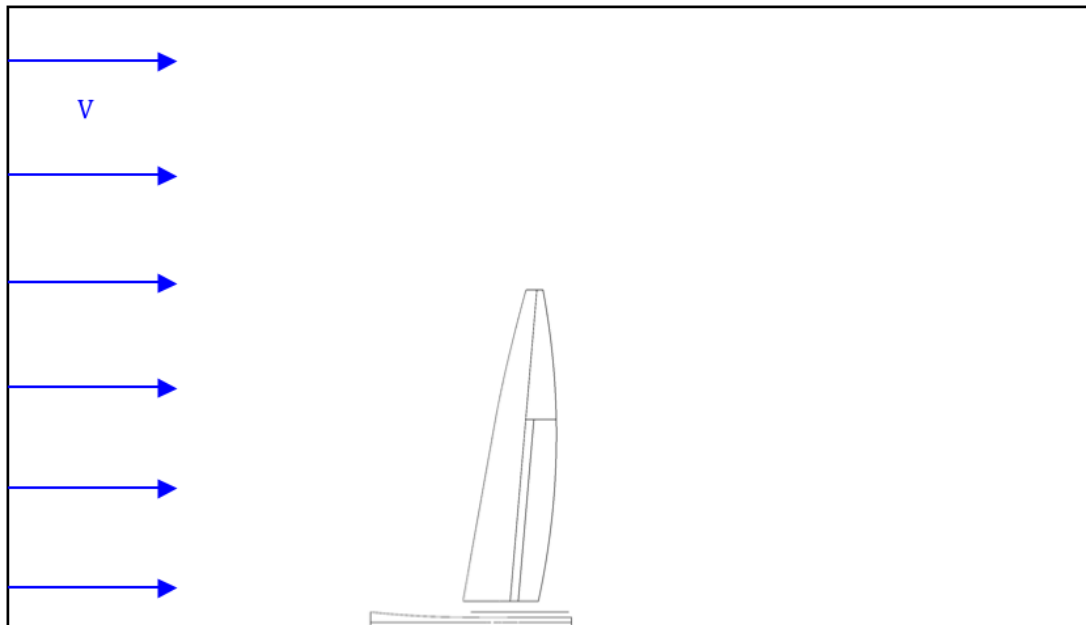


Figure 3.15: Definition of the velocity inlet

Chapter 4

Results and Analysis

4.1 2D Simulations

As concluded during the mesh generation process and indicated in the literature review the $k - \epsilon$ model provides sufficient results (see Appendix E). Thus the results presented in this chapter are of the $k - \epsilon$ model.

4.1.1 Polars

The polars reflect the wing theory (described in section 2.1.3); that is, the increase of flap deflection increases the C_l for fixed AoA , but decreases the AoA of $C_{l_{max}}$. Presented on the following page are the polars of C_l and C_d for flap deflections of 10° , 15° and 20° (figures 4.1 and 4.2 respectively). The figures for flap deflections of 35° , 40° and 45° are attached in section 4.7 (see figure 4.15 and 4.16 respectively). These are the results for the current setup of the wing with a gap of 3%.

The gap setup only affects the trailing edge at high flap deflections. The ‘fingers’ don’t touch the trailing edge at flap deflections of 10° and 15° i.e. it is on original symmetric shape and not morphed. The gap of 10° and 15° flap deflection is $< 2\%$. The angle of the flap deflection is denoted in the form of f20 (for flap deflection of 20° in this case) in the graphs.

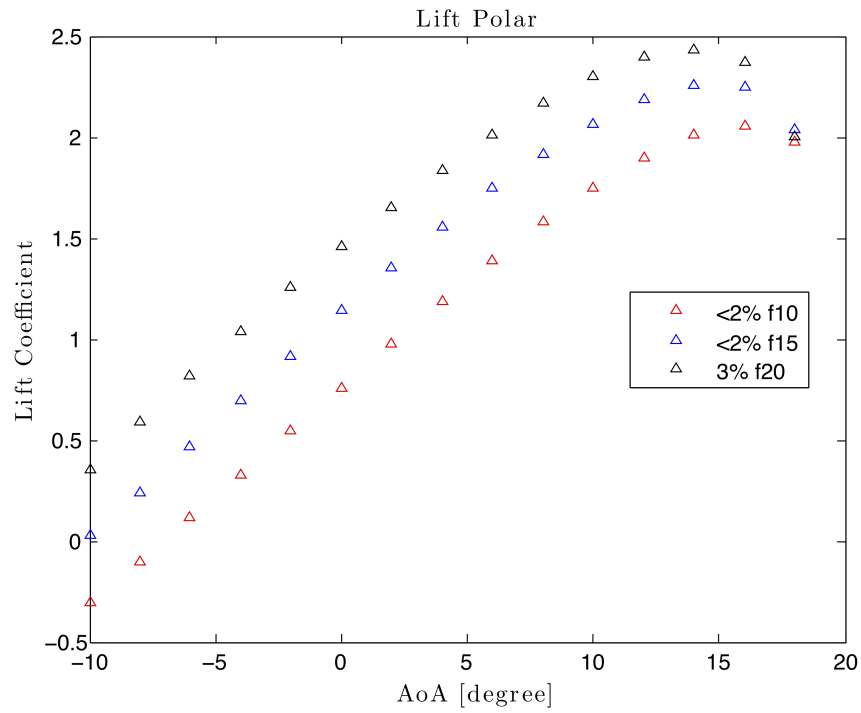


Figure 4.1: Polars for flap deflection of 10° , 15° and 20°

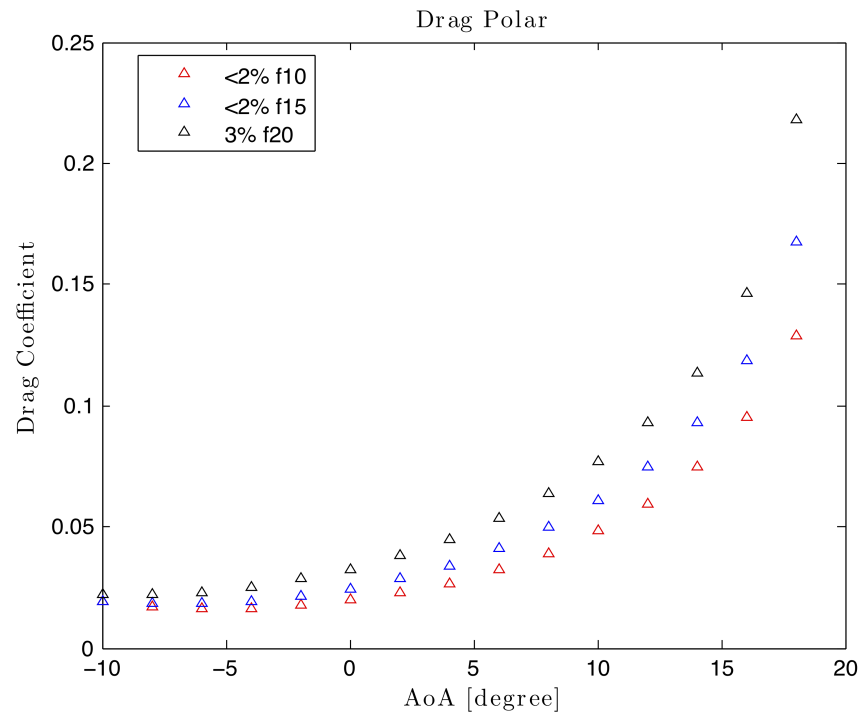


Figure 4.2: Polars for flap deflection of 10° , 15° and 20°

4.1.2 Gap Effect

All cases were run with three different gap settings. The original gap setting of the wing was 3% of main chord. Cases were run with gap sizes of 2%, 3% and 4% of main chord. Recall that the change in gap size does not have an effect for the most part on the shape of the trailing edge of the main wing section for low flap deflection. The change in shape of the trailing edge becomes apparent at high flap deflections.

C_l and C_d polars comparing the gap settings of 2%, 3% and 4% at a flap deflection of 40° are given in figure 4.3 and 4.4, respectively. Figures 4.5, 4.6 and 4.7 are streamline visualisations for the three different gap settings at an AoA of 4° and a flap deflection of 40° .

The figures (4.8, 4.9 and 4.10) representing the flow field around the flap for a gap setting of 3% of main chord at an AoA of -20° , -14° and 4° degrees (with a flap deflection of 40 degrees). The red arrow indicates the point of separation.

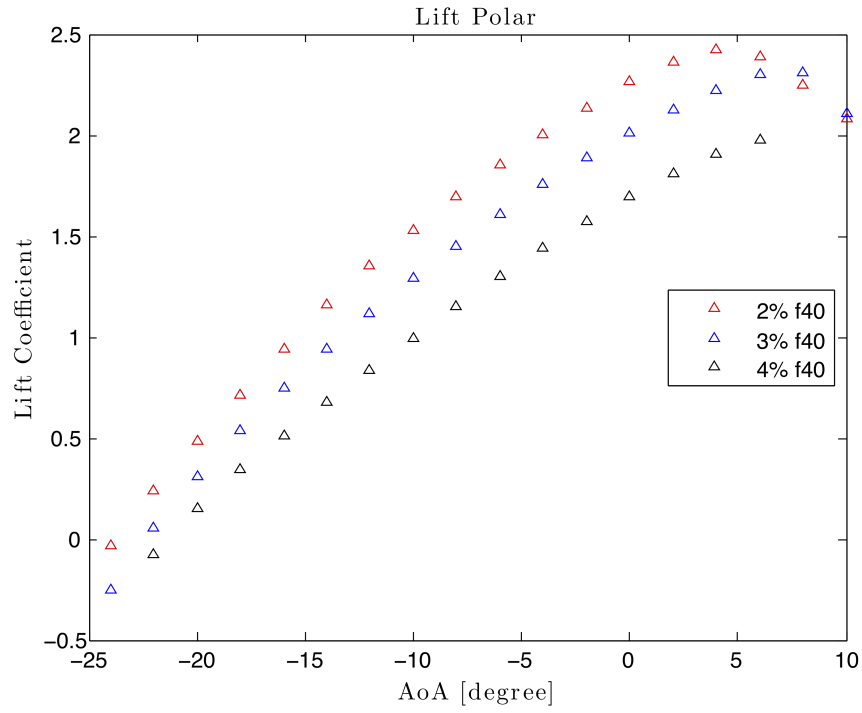


Figure 4.3: C_l polar for a gap of 2%, 3% and 4% at flap deflection of 40°

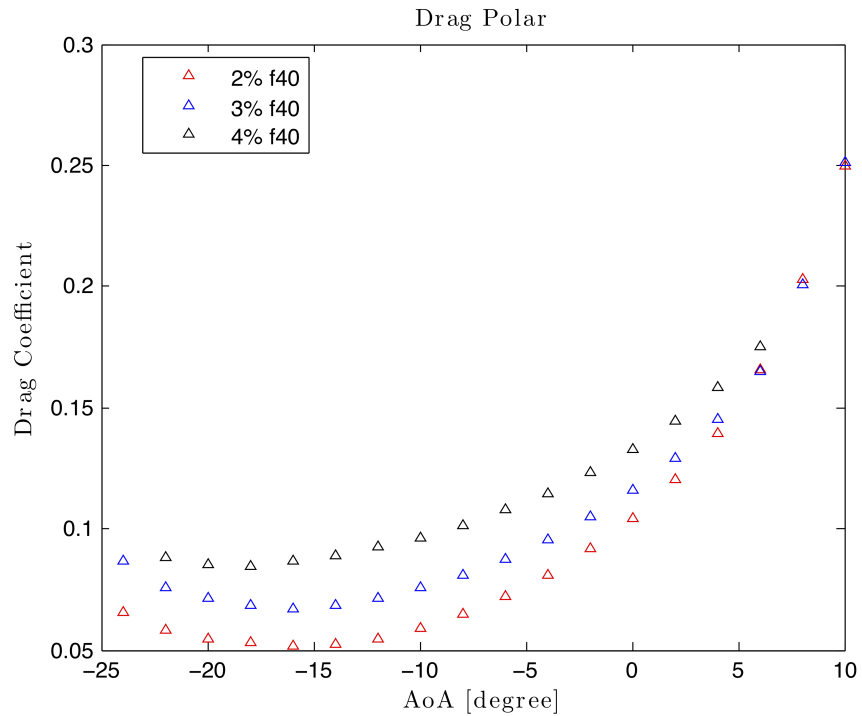


Figure 4.4: C_d polar for a gap of 2%, 3% and 4% at flap deflection of 40°

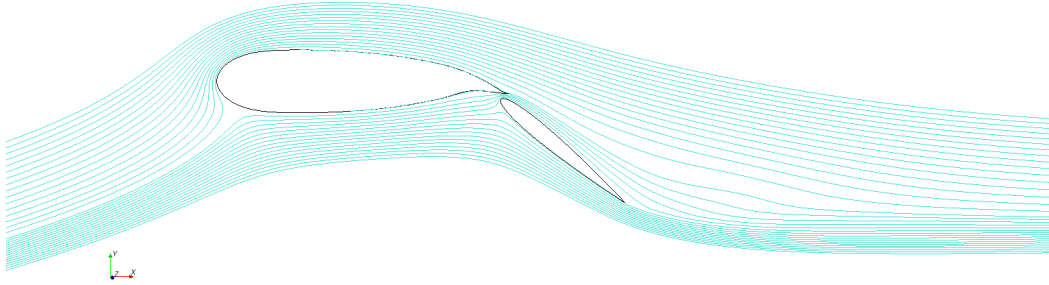


Figure 4.5: Stream lines for a gap of 2% with a flap deflection of 40° at AoA of 4°

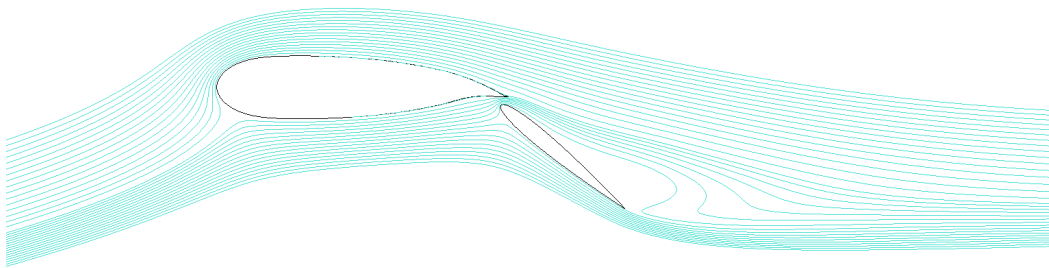


Figure 4.6: Stream lines for a gap of 3% with a flap deflection of 40° at AoA of 4°

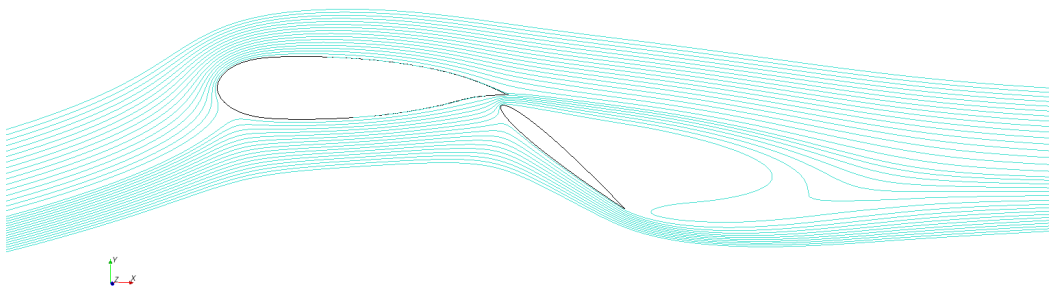


Figure 4.7: Stream lines for a gap of 4% with a flap deflection of 40° at AoA of 4°

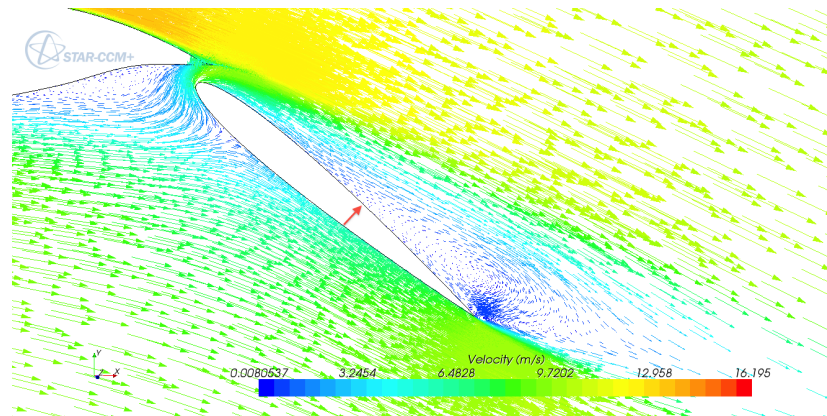


Figure 4.8: Flow field around flap for 3% gap with flap deflection of 40° at AoA of -20°

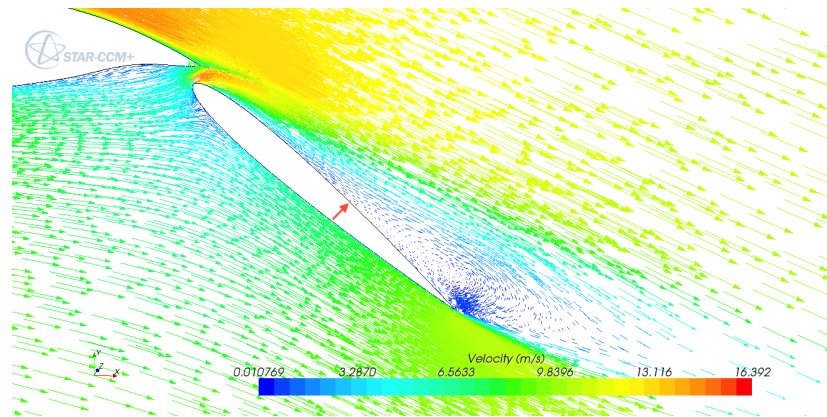


Figure 4.9: Flow field around flap for 3% gap with flap deflection of 40° at AoA of -14°

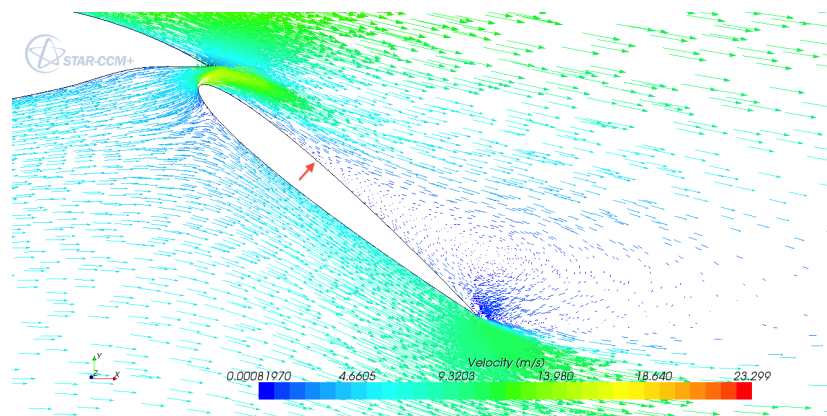


Figure 4.10: Flow field around flap for 3% gap with flap deflection of 40° at AoA of 4°

The polars of C_l and C_d for flap deflections of 35° and 45° are shown in figures 4.17, 4.18, 4.19 and 4.20, respectively.

Recall figure 3.2; due to the sliding skins at the trailing edge, the skin extends beyond the leading edge of the flap at high flap deflections. With a gap of 2% of main chord this effect is exaggerated; this results in a velocity vector that is parallel to the profile surface after the leading edge. This results in a flow that stays attached around the flap (and main wing section) for all required flap deflections and $AoAs$, and achieves higher C_l and reduced C_d than with a bigger gap setting, as shown in figure 4.3 and 4.4, respectively.

With a gap $> 2\%$ the skin of the trailing edge does not extend as much beyond the leading edge of the flap. This results in a velocity vector that is no longer parallel to the profile surface, see figures 4.8, 4.9 and 4.10. This results in a flow that becomes less attached to the flap with increasing AoA , as shown in figures 4.5, 4.6, 4.7, 4.8, 4.9 and 4.10. The partially detached flow shows a drop in the prediction of C_l and an increase of C_d compared to the prediction with a 2% gap, as shown in figures 4.3, 4.4, 4.17, 4.18, 4.19 and 4.20

4.1.3 Effect of discretisation scheme

During the mesh generation process it was discovered that not all cases with gap settings of 3% and 4% converged with second order up-wind discretisation for mass and momentum (see section 3.4). The cases with high flap deflection (35° , 40° and 45°) did however converge when first order up-wind discretisation for mass and momentum was used. This indicates numerical oscillations with the second order up-wind discretisation that could be stabilised by the diffusive first order up-wind discretisation.

Figures 4.11 and 4.12 show the C_l and C_d predictions for the cases with a gap setting of 2% and flap deflections of 40° , respectively.

The polars indicate that the first and second order discretisation agree in their predictions in the early (linear trend) values for C_l . The first-order discretisation predicts lower C_l values for AoA 's greater than -14° . The second-order discretisation C_l values stay linear until an AoA of -12° . For greater AoA , values of C_l are predicted to be slightly smaller with the first order discretisation than the second order discretisation.

As the main interest lies in the 'linear' C_l region, the results with the first-order discretisation are accurate for the purpose of the data use.

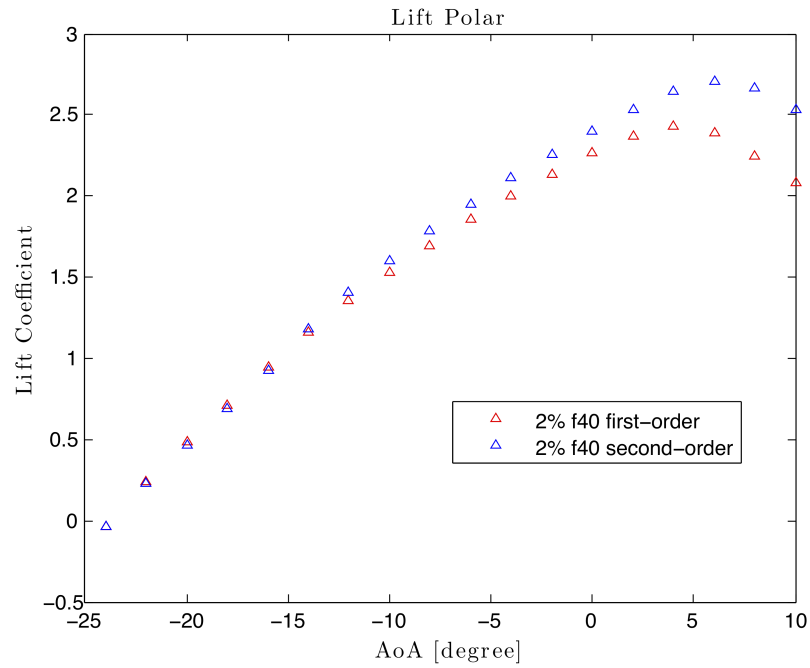


Figure 4.11: C_l polars comparing first and second order discretisation of mass and momentum

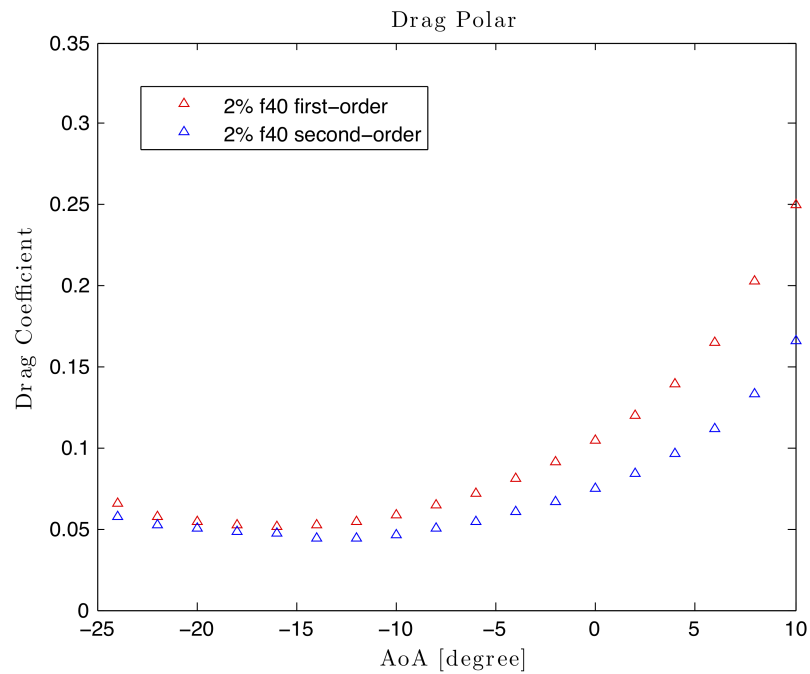


Figure 4.12: C_d polars comparing first and second order discretisation of mass and momentum

4.2 Remarks about the turbulence models

As shown in the literature review and Appendix E the $k - \epsilon$ model performs well in the lower linear C_l region. The $k - \epsilon$ proved to be very robust for partially separated flows.

During the mesh generation process it was shown that the SST model was not very robust for cases with partially separated flows, confirming the findings in the literature review.

4.3 Further analysis of Profile data

The initial plan was to deliver data before the IC^4 (International C Class Catamaran Challenge) in September 2010. This data was to be used by a VPP that was developed by a third party. The idea was to evaluate the setup of the wing with the VPP to obtain an optimum configuration.

However, by the time of the race the VPP was not delivered to Team Invictus. Only with a VPP the apparent wind angle, the optimal AoA and flap deflection can be predicted. However the data itself can give an indication as to which gap is more efficient with out further evaluation with a VPP. As the data indicated **the flow stays attached longer with a smaller gap setting.**

4.4 IC^4 2010 - the race

With the data provided it was suggested to Team Invictus to change the gap setting of the wing. The race had six contenders that year. During the initial fleet races two boats separated them selves from the rest of the fleet with superior performance. Those two boats went on to match races to decide the winner of the championship. The remaining boats carried on competing in fleet races to decide the lower race places. Team Invictus was on third place for the major part of the races, resulting in a third place overall.

Halfway though the competition the team decided to implement the recommendations of this project and changed the gap to 2%. This led to significant performance improvement on downwind legs.

The two boats at the front of the fleet both had relatively thin wings and smaller hulls compared to the rest of the fleet. Also the crew on those two boats

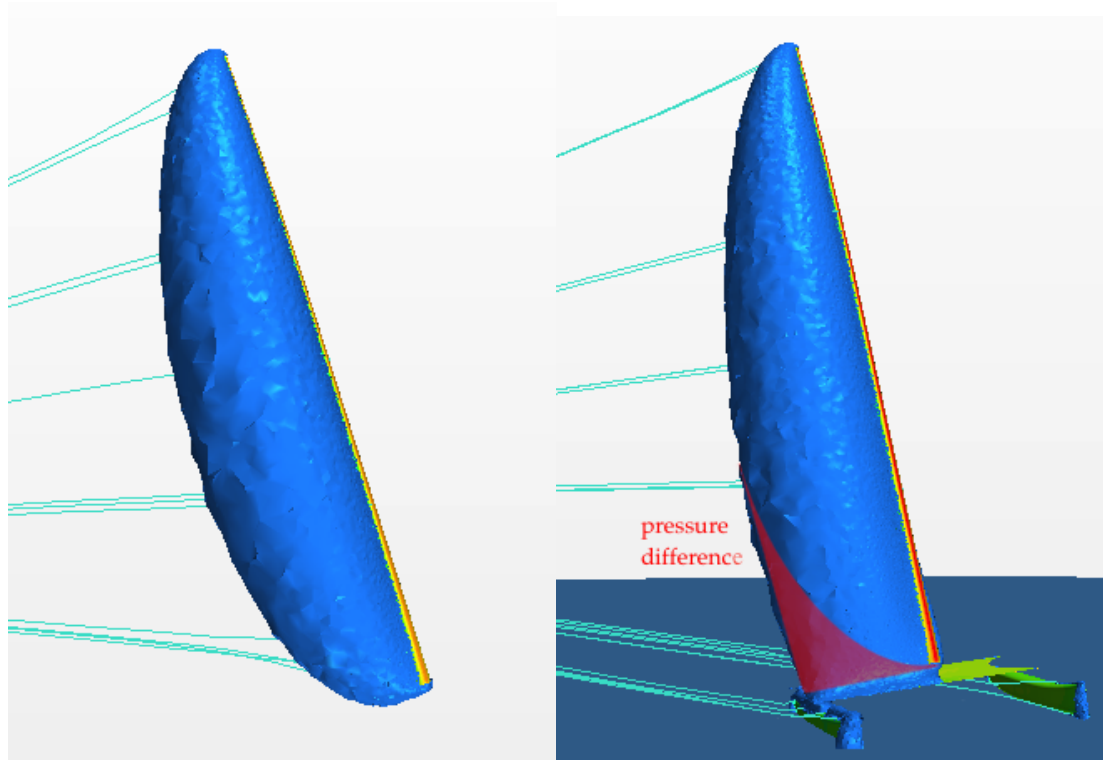
were world class catamaran sailors. The thinner wings proved to perform better up wind, but the major advantage of those two boats was probably also due to the very experienced catamaran crew those two boats had.

The event was regarded as a major success by the team. Team Invictus is now eager to hold the next event and build a new competitive boat.

Implementing the recommendation of this research during the race quantifies the findings of this work with a significant performance improvement of the boat. **This supports the findings and supports the decisions made during this research.**

4.5 3D wing results and analysis

This preliminary study provides a flow visualisation of the effect of the boat hulls on the flow around the sail.



(a) Low pressure area on wing

(b) Low pressure area on wing with boat (green)

Figure 4.13: Visualisation of a pressure isosurface (for the same pressure value in both figures) and streamlines; the red overlay in (b) visualises the difference in the pressure isosurface.

As visualised in figure 4.13 the boat has an effect on the pressure distribution on the wing. By visual comparison it appears that the lift of the wing is altered from the root to about half span of the wing. This has a significant effect on the overall lift generated by the wing as shown in figure 4.14. The lift generated with the boat underneath the wingsail is about $\approx 10\%$ higher than the wing alone.

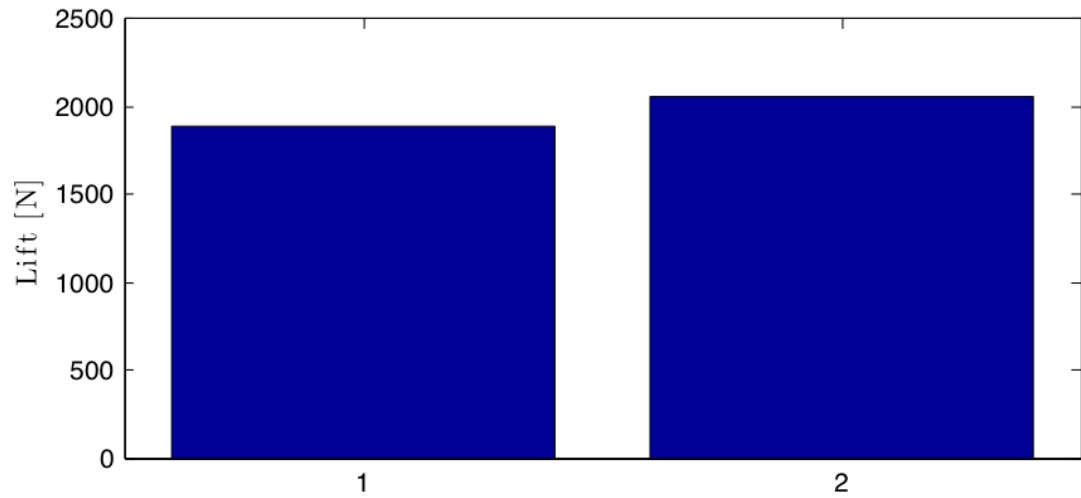


Figure 4.14: Lift generated by (1) the wing alone (2) the wing with boat and water.

A concern by Team Invictus was the size of the gap between the trampoline (the fabric between the two hulls to support the crew) and the root of the wing. This gap was thought to have a significant effect on the lift distribution and was kept as small as possible. This introduces a problem at gybing and tacking, when the crew needs to go across the trampoline underneath the wing.

The gap between the root of the wing and the trampoline seems to have only a small effect on the lift distribution, as shown in figure 4.13. However further analysis is required to determine how the gap sizes affect the lift of the wing.

4.6 Conclusion

The following key findings were made during this research:

- The size of the gap between the leading edge of the flap and the trailing edge of the main wing section has a significant effect on the flow around the flap.
- The boat underneath the wingsail effects the pressure field around the wingsail and the lift generated by the wingsail compared to the wing alone.

With a gap of $\geq 3\%$ (of main wing section chord) the flow starts to separate at the flap with increasing AoA and flap deflection. With a gap of 2% (of main wing section chord) the flow stays attached to the flap at high AoA and flap deflection. The with attached flow, higher C_l and lower C_d values of the wing section were achieved.

As shown in the literature review the results confirm that the data is accurate in the lower linear C_l region. With increasing AoA the predictions become more inaccurate. The point of stall is assumed to be predicted too late. With the data shown in Appendix E and findings in the literature review, the point of separation is assumed to be under predicted. Without knowing the exact point of separation the general trend of the effect of the gap size can be shown.

The data was sufficient as the performance improvement during the 2010 IC⁴ showed.

The flow visualisation around the wingsail indicates, that boat and water have an effect on the lift distribution. **This preliminary study indicates that the lift distribution can be modelled as a semi-span in a VPP** (see section 2.2.6 where this question was raised). However further analysis is required as to the gap size between the root of the wing and the trampoline that is practical without altering the lift distribution significantly. Further more, the increase of drag due to the boat was not considered in this study and requires further investigation.

This research shows that the $k - \epsilon$ model provided sufficient solutions when applied to the lower ‘linear’ lift region. Potential short comings are the stall predictions with this approach as shown in appendix E.

4.7 Figures

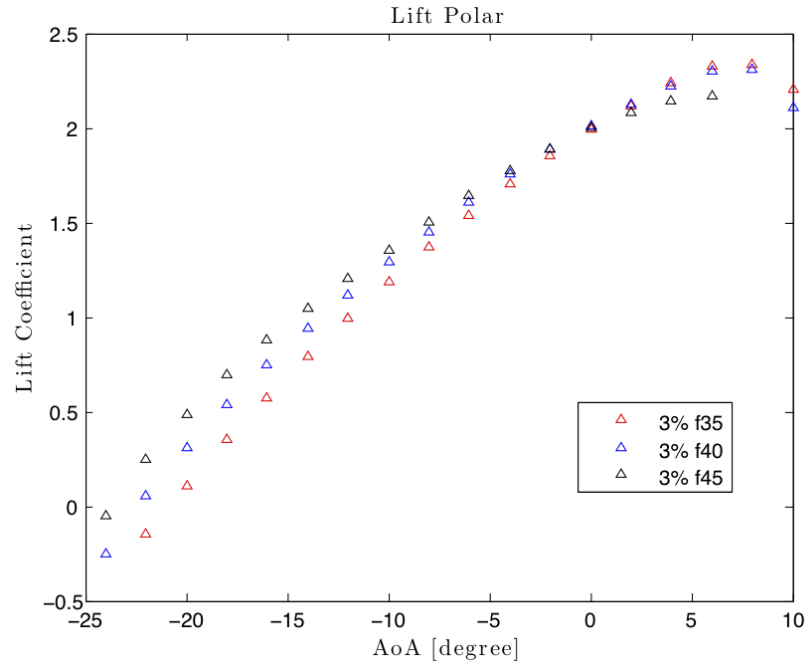


Figure 4.15: Polars for flap deflection of 35°, 40° and 45°

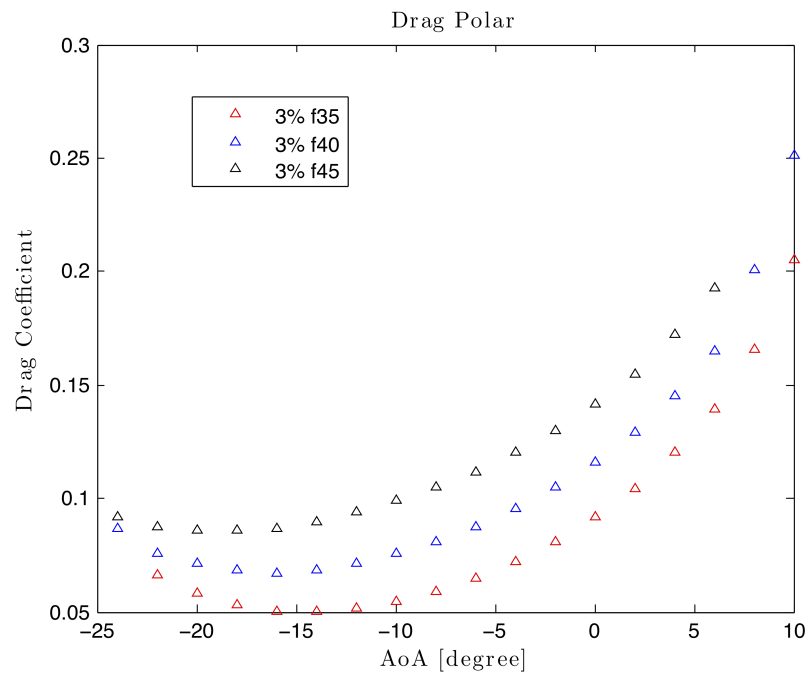


Figure 4.16: Polars for flap deflection of 35°, 40° and 45°

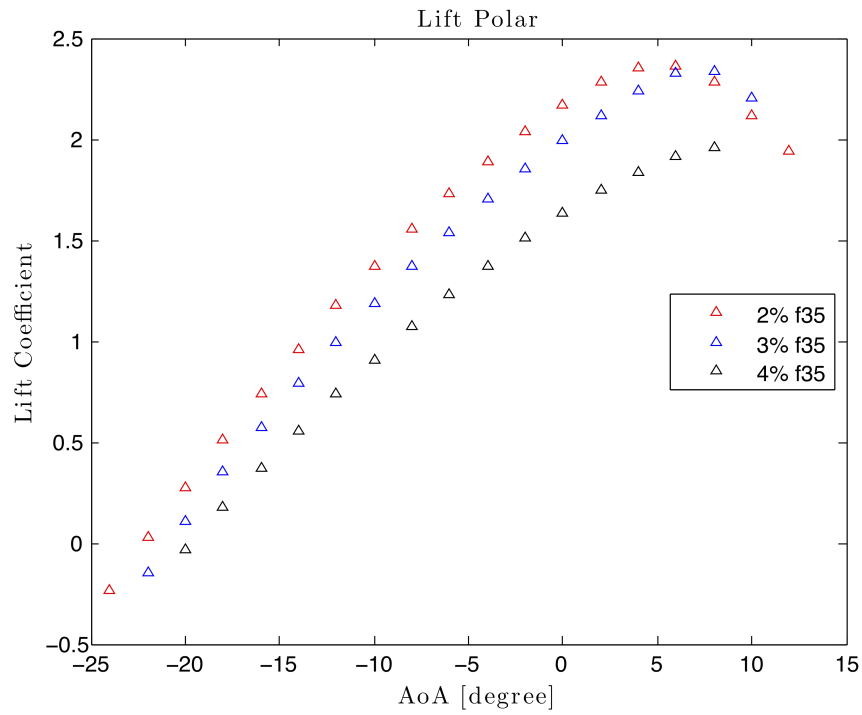


Figure 4.17: Polar for gap of 2%, 3% and 4% at flap deflection of 35°

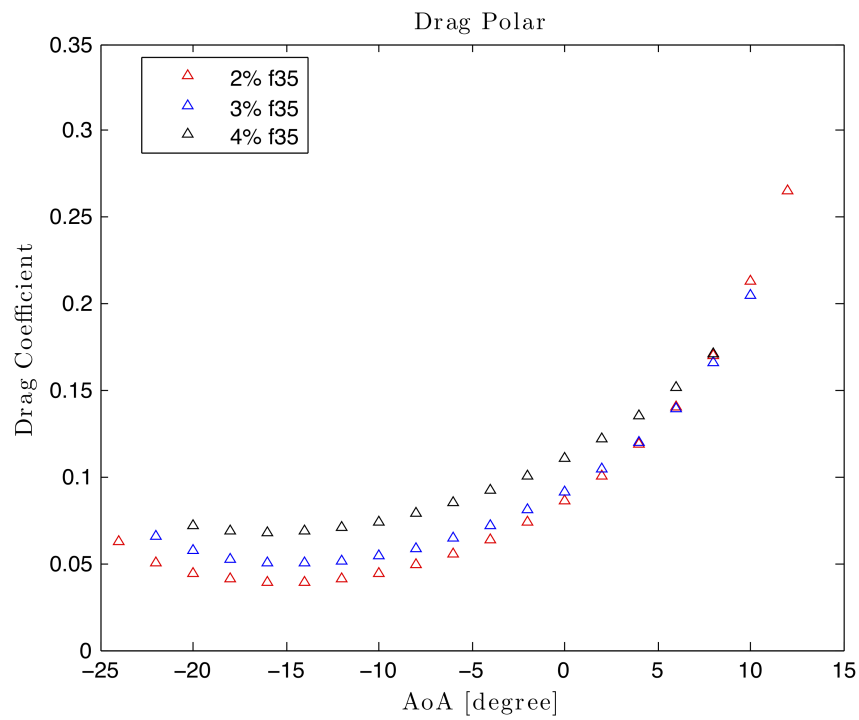


Figure 4.18: Polar for gap of 2%, 3% and 4% at flap deflection of 35°

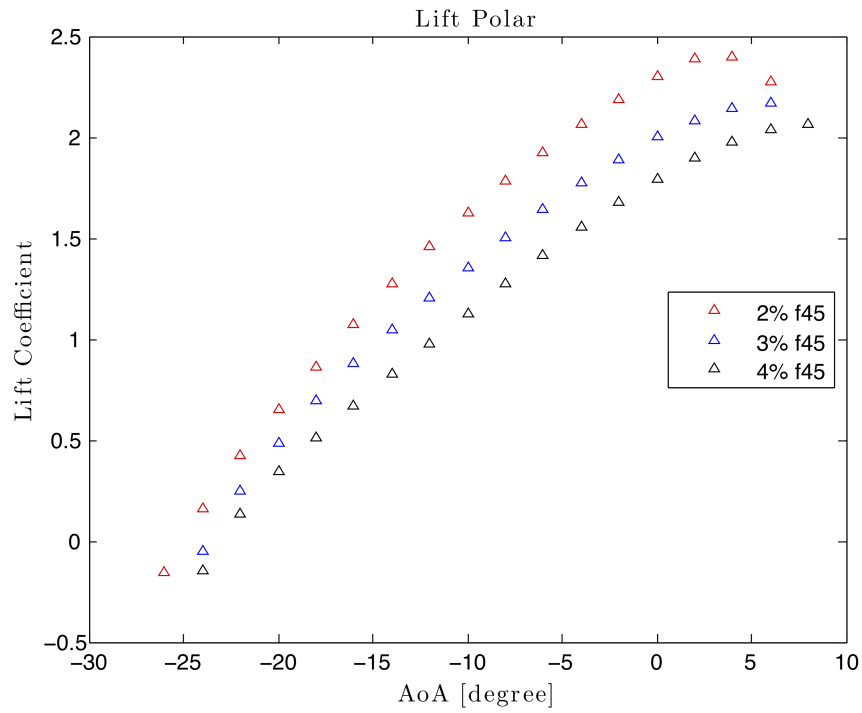


Figure 4.19: Polar for gap of 2%, 3% and 4% at flap deflection of 45°

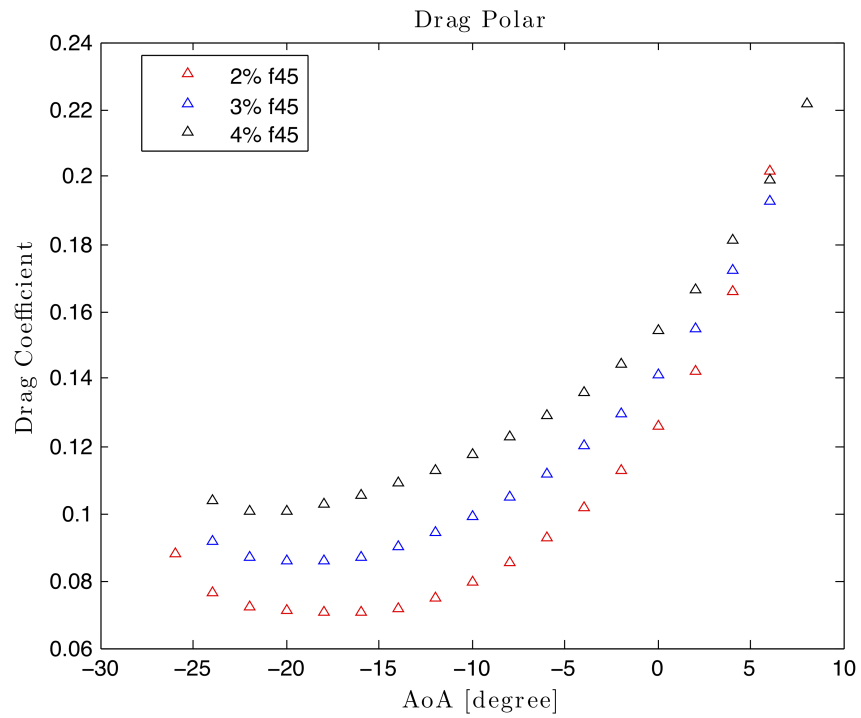


Figure 4.20: Polar for gap of 2%, 3% and 4% at flap deflection of 45°

Chapter 5

Future work

5.1 Turbulence model selection

For initial analysis the $k - \epsilon$ model provides good stability and reasonably good results for attached flows. However for a more accurate drag predictions of attached flows the SST model may be more suitable as shown in Appendix E and [23].

5.1.1 Turbulence of wind

Ross [34], in regarding the C-Class development points out that the atmospheric boundary layer is very turbulent, with a high turbulent intensity. However no references are given for measurements. For a more accurate modelling of the flow around the wingsail the turbulent intensity as a function of height is required to improve the inlet conditions.

5.2 Separated flow cases

The cases with partially or fully separated flow should be run in time-dependent mode to obtain more accurate solutions. The $k - \epsilon$ model provides a steady solution for partially and some fully separated flow cases, however this is due to the model ‘smearing’ out the oscillations and thus giving a solution that is physically inaccurate. The $k - \omega$ SST or RSM are often more accurate in time-dependent mode.

5.3 Point of separation

For an accurate prediction of the point of separation a different turbulence modelling approach is required. The fundamental problem of EVMs is, they either over or under predict the point of separation. Also the drag prediction in the stall region becomes less accurate. Thus a modelling approach such as RSM or LES is required for stall and post stall predictions.

5.4 Flap leading edge location

The current case includes an effect of an overlap of the trailing edge of the main wing section over the leading edge of the flap. Further analysis is required to optimise the overlap.

5.5 Root wing tip gap size

The root gap size requires further analysis for future wingsail designs. The problem is, that a small gap is required to minimise the root tip vortex and thus minimise the lift reduction in this area. On the other hand the gap needs to be big enough for the crew to move across the boat on a tack or gybe. Further more the effect of the velocity profile on the root vortex needs further investigation.

5.6 Wing/Chord ratio

For future designs an optimisation study is required to determine the optimum wing/chord ratio.

5.7 Wing profile analysis

As proven in the 2010 IC⁴ race, thinner wings provide superior performance, especially up-wind. However it was also shown that the thicker wing of Team Invictus was able to keep up with the two thinner wings on the down-wind legs.

For a better performing thin wing the stall must be delayed to achieve higher $C_{l_{max}}$ values. A morphing leading edge could achieve this by forming a high radius

leading edge on the suction side (such as the leading edge shape of the current wing in this study) [12].

5.8 Wingsail twist

With the presence of accurate apparent wind prediction of a VPP, a study for the optimum active wing twist is required for compensating the change in apparent wind with height.

5.9 6-degree-of-freedom simulation

The VPP relies on theories to predict lift distribution and hull drag. This introduces an error due to the theory. To eliminate this error a 6 DOF (6-Degree-Of-Freedom) simulation (coupled aero-hydro simulation) would be required. However the computational power and time requirement for this type of simulation makes a VPP currently more viable for quick predictions.

References

- [1] Monofoil, 2010. URL <http://www.monofoil.com/>.
- [2] Vestas Sailrocket, 2010. URL <http://www.sailrocket.com/>.
- [3] Wotrocket, 2010. URL <http://www.wotrocket.com/>.
- [4] Ira H. Abbott and Albert Edward Von Doenhoff. *Theory of wing sections: including a summary of airfoil data*. Courier Dover Publications, 1959.
- [5] Kenneth Abel. Application Notes: A Reversible Asymmetry Rigid Aerofoil For Sailing Vessels, 1980.
- [6] John D. Anderson. *Fundamentals of Aerodynamics*. McGraw Hill Higher Education; 4th edition, 2006.
- [7] D. W. Atkins. *CFD assisted design and experimental testing of a wingsail with high lift devices*. PhD thesis, Salford, 1996.
- [8] Frank Bethwaite. *High Performance Sailing*. Adlard Coles Nautical, July 2007.
- [9] J. Blazek. *Computational fluid dynamics: principles and applications*. Elsevier Science, 2001.
- [10] Vera Boome and Olivia Stodleck. Team Invictus, 2010. URL <http://www.teaminvictus.com/>.
- [11] CD-adapco. Star-CCM+ 4.04.011, 2009.
- [12] Julien Chaussée. Team Invictus. private communication, 2009.
- [13] S. Collie, M. Gerritsen, and M. O’Sullivan. Numerical Simulation of the turbulent flow past Upwind Yacht Sails. *Journal of Wind Engineering and Industrial Aerodynamics*, 91(2):185–197, 2002.

- [14] A. Daif, B. Kamoun, and M. Mudry. Evaluation of wingsail interactions for windship propulsion. *European Journal of Mechanics*, 10(2):185–206, 1991.
- [15] D. Detomi, N. Parolini, and A. Quarteroni. *Mathematics in the Wind*, 2009.
- [16] Joel H. Ferziger and Milovan Peric. *Computational Methods for Fluid Dynamics*. Springer, 3rd, rev. edition, November 2001.
- [17] Fabio Fossati. *Aero-hydrodynamics and the Performance of Sailing Yachts: The Science Behind Sailing Yachts and Their Design*. Adlard Coles Nautical, December 2009.
- [18] James Grogono. *Icarus: the Boat that Flies*. Adlard Coles Nautical, 1987.
- [19] W P Jones and B E Launder. The prediction of laminarization with a two-equation model of turbulence. *International Journal of Heat Mass Transfer*, 15:301–314, 1972.
- [20] M. Khayyat and M. Rad. Comparison Final Velocity for Land Yacht with a Rigid Wing and Cloth Sail. In *Proceedings of the World Congress on Engineering*, volume 2, 2008.
- [21] Steve Killing. Alpha and Rocker - Two Design Approaches that led to the Successful Challenge for the 2007 International C-Class Catamaran Championship. In *The 19th Chesapeake Sailing Yacht Symposium*, number March, 2009.
- [22] A N Kolmogorov. The equations of turbulent motion in an incompressible fluid. *Izvestia Acad. Sci., USSR; Physc*, 6:56–58, 1942.
- [23] W Lasher and J Sonnenmeier. An analysis of practical RANS simulations for spinnaker aerodynamics. *Journal of Wind Engineering and Industrial Aerodynamics*, 96(2):143–165, February 2008. ISSN 01676105.
- [24] B E Launder and B I Sharma. Application of the energy-dissipation model of turbulence to the calculation of flow near a spinning disc. *Letters in heat and mass transfer*, 1:131–138, 1974.
- [25] B. E. Launder, W. Morese, W. Rodi, and D. B. Spalding. NASA SP-321. In *Langley Free Shear Flow Conference*, pages 361–426, 1972.

- [26] Mike Lennon. UK International Moth Site, 2010. URL www.internationalmoth.co.uk.
- [27] P.B.S. Lissaman. Lift in a Sheared Flow. volume 33, pages 141–148, 1986.
- [28] James F. Manwell, Jon G. McGowan, and Anthony L. Rogers. *Wind Energy Explained: Theory, Design and Application*. Wiley-Blackwell, April 2002.
- [29] Czeslaw A. Marchaj. *Aero-Hydrodynamics of Sailing*. Intl. Marine Pub., January 1989.
- [30] Medina Yacht CO LTD. Outlook for Wind Assistance. *Journal of Wind Engineering and Industrial Aerodynamics*, 19, 1985.
- [31] F R Menter. Two-Equation Eddy-Viscosity Turbulence Models for Engineering Applications. *AIAA*, pages 1598–1605, 1994.
- [32] Stephen B. Pope. *Turbulent Flows*. Cambridge University Press, 2000.
- [33] V. Radhakrishnan. From square sails to wing sails: The physics of sailing craft. *Current Science*, 73(6):503–516, 1997.
- [34] J. C. Ross. Aerodynamic Design of a Rigid-Wing Sail for a C-Class Catamaran. In *The Ancient Interface XVIII, Proceedings of the Eighteenth AIAA Symposium on the Aer/Hydronautics of Sailing*, volume 35, pages 17–27, 1989.
- [35] J. Otto Scherer. Aerodynamics of High-Performance Wing Sails. *Marine Technology*, 2(3):270–276, 1974.
- [36] Septentrion Communication. Hydroptère, 2010. URL www.hydroptere.com.
- [37] Robert E. Sheldahl and Paul C. Klimes. Aerodynamic Characteristics of Seven Symmetrical Airfoil Sections Through 180-Degree Angle of Attack for Use in Aerodynamic Analysis of Vertical Axis Wind Turbines, 1981.
- [38] Lou Vest. A-Cat primer, 2008.
- [39] Frank M. White. *Fluid Mechanics*. McGraw Hill Higher Education; 6th Revised edition edition, 2009.
- [40] D C Wilcox. Turbulence Modelling for CFD. Technical report, DCW Industries Inc, La Canada, CA, 1994.

Appendices

Appendix A

Terms used in sailing

Luff is the upwind edge of a sail.

Leach is the downwind edge of a sail.

Batten is a semi flexible enforcement in the sail that runs horizontally from the leach upwind.

Reefing is reducing the sail area.

Una rig is rig with only one sail.

Heading the direction the boat points to.

Windward is facing the wind.

Leeward downwind facing.

Tacking is changing the sailing direction by turning the bow (front of a boat) through the wind. This method is used for going upwind.

Gybing is changing the sailing direction by turning the stern (rear of a boat) through the wind. This method is used for going down-wind.

Reaching is sailing a course of about 90° to wind.

Broad-reaching is sailing on a course to wind that would nearly coincide with a gybing course.

Heeling is the boat rolling about its longitudinal axis.

Appendix B

Historical background of sailing

B.1 From drag to lift

Sailing, a practice reaching back to 2000 BC [33]. In those ancient days the Egyptians were transporting goods up and down the Nile river. The river, is running from south to north with prevailing winds north to south. Thus the boats were drifting down stream and a fabric/sail was hoisted to go up the stream against the current.

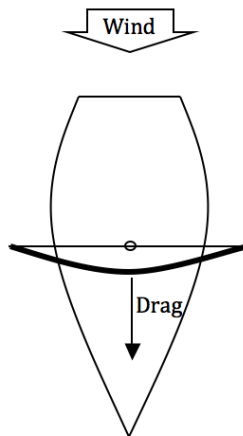


Figure B.1: Downwind sailing due to aerodynamic drag

This form of sailing relies purely on the aerodynamic drag generated by the hoisted fabric. With this practice only one direction could be sailed - downwind, see figure B.1.

With this configuration the theoretical maximum speed can only be as high as the wind velocity. However before this speed can be attained the increasing

hydrodynamic drag must be equalised. The hydrodynamic drag is a sum of skin friction drag, form drag and wave making drag. The first two increase with the square of the boat speed when flow is turbulent.

In the era of the square riggers the sail area increased to overcome the hydrodynamic drag. Although they were able to adjust sail attitude those boats were only able to go slightly higher as reaching i.e. 90 degrees to the wind. With the huge sail area those boats proved the increasing wind easily can be destructive and reefing was anything but easy. Sailors were lost in reefing procedures.

The Chinese had a different approach to sailing long before the Western world [33], they were able to reef easily and were able to go much higher than reaching.

Since the invention of the steam engine sailing is mainly a activity of sportsmen. Sailing became a sport, regattas are held till present time, where sailing boats are competing over a course to be the fastest.

In the 18th century a prediction by Lord Rayleigh changed how sails are used. He predicted, that the force produced by a lamina at small angle in a flow increases to the square of the sine of the angle i.e. lift. This changed the design and use of the sail.

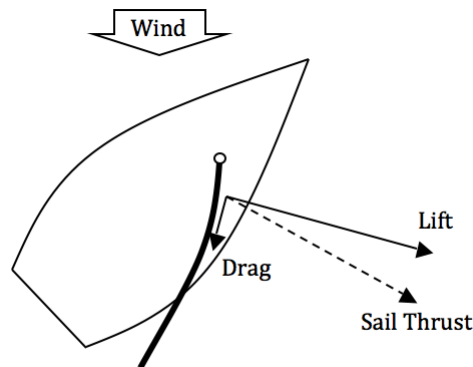


Figure B.2: Forces generated by a sail

This use of a sail made it possible to close reach and tack upwind. The generated lateral force required lateral stabilisers, e.g. keels.

B.2 From sail to wingsail

For thousands of years a sail (by definition any flexible material extended on a rig) has been used. Since the first flight by mankind the development of aerofoils

started. Soon after the analogy of Lift and Drag between an aerofoil and a sail was made and the idea of a wingsail was born.

In the 80s research had been undertaken in the field of wingsails for commercial use [14, 30], triggered by rising oil prices [7]. However this research was focused on the feasibility of propulsion of large vessels by wind energy not on high performance wing-sailing.

The wingsails known today are mainly developed for speed records in sailing or in competitive class sailing.

Speed sailing Those wings are designed for very specific wind conditions and wind angles (for a speed record the set distance must be sailed in both direction). Thus, those wings (and hull off the boat) are tailored for maximum efficiency on one single course (reaching).

Competitive sailing For this type of sailing the performance focus is on upwind/close-reach, reach and broad-reach/down-wind sailing.

In recent years the sailing speed record projects like 'Sailrocket' [2] and 'Wotrocket' [3] were building wingsail designs in an attempt to become the fastest sailing boat over 500 metres. Another noteworthy project is 'Monofoil' [1]. This project aims to build a vessel that can travel at 100kts over water with wind propulsion.

Only in recent years wingsails have made an appearance at regattas and match racings other than in the C-Class, like in the A-Class [38] and last year's 33th America's Cup.

In leisure and touring sailing, wingsails still haven't caught on mainly due to the following argument: An ongoing argument is, that wingsails can not be reefed easily, thus unfit for use as an alternative to conventional sails [5]. Whereas conventional sails are easily reefed in strong winds to reduce the heeling moment. The counter argument is that a wingsail at an AoA (Angle of Attack) such that $C_l = 0$ produces less drag force than the rig of a soft sail [8, 35]. However, this would require a free rotating wingsail and the wind direction changes over time especially in stronger winds with gusts. Thus the latter argument is somewhat weak when it comes to practice.

The development of the wingsail as it is known today in high-performance sailing started with the definition of catamaran development classes in the early 60s. This was triggered by a claim of an American to have build the 'fastest small sailing boat in the world'. In order to compete on common grounds four

catamaran development classes were formulated. Those classes (A, B, C and D-Class) only restricted the developers by maximum width, maximum length and maximum sail area. Those for classes only distinguished each other in consecutive sizing.

The A-Class is nowadays simply referred to as A-Cat, a single handed catamaran. The developments in the B-Class lead to various double handed cats still raced in regattas around the world (like the Olympic tornado class, Hobie 16s and Formula 18s). D-Class catamarans rare one off productions make appearances around the world, this class is a big three crew catamaran. The C-Class made a slightly different development throughout the years.

Appendix C

Hydrofoils in the C-Class

Since the C-Class has been the forefront of aerodynamics in sailing, one may wonder why hydrofoils are not used in this class. The *International Moth* class (see figure C.1a) is currently a very successful ‘foiling class’, demonstrating the advantage of hydrofoils on small dinghies. Also the speed sailing record holder *l’Hydroptère* uses hydrofoils (see figure C.1b).



(a) foiling ‘Moth’ [26]



(b) ‘l’Hydroptère’ (copyright Beken of Cowes) [36]

Figure C.1: Boats sailing with hydrofoils

The moth is a development class. The hull used to be much like a flat hull similar to the current ‘International Europe’ class, since they used to be one class before they separated and the moth developed further. For a mono hull the drag increases rapidly with speed until (depending on hull shape) the hull is forced to plane (i.e. produces the required lift by the dynamic displacement of the oncoming water). Thus getting the hull out of water and reducing the hull drag early is crucial for monohull boats. For a hydrofoil the drag only increases very

little with speeds up to 40 kts [18] and is therefore more efficient for monohull boats.

Nevertheless the drag still increases with speed. In 1969 hydrofoils were fitted to a catamaran [18] (a *tornado* or B-Class catamaran), with the name ‘Icarus’, was mainly aimed at speed sailing rather than competitive sailing around a course. This catamaran won the world sailing speed record 13 times in the class, proving the concept of maximising the top speed of a catamaran with hydrofoils. However, ‘Icarus’ never raced around a course against a standard non-foiling *tornado* class boat.

To date no catamaran with hydrofoil has taken part in a IC^4 (International C-Class Catamaran Championship). Grogono postulates that hydrofoils would decrease the hull drag of a C-Class catamaran in the range of 15 - 35 kts [18]. However at speeds below 15 kts the hull would be in the water and, due to the hydrofoil construction, producing more drag, thus reducing the performance of the boat in light winds.

For the 2007 challenge a Canadian team developed two identical boats ‘Alpha’ and ‘Rocker’ with the same hulls and wing but with one boat fitted with hydrofoils. With their success in the moth class and Grogono’s proposal for a hydrofoil c-class catamaran [18]. Unfortunately ‘Rocker’ with T-foils (a hydrofoil fitted at half span to the bottom of a centre board looks like an inverted ‘T’, hence the name) never matched the performance of ‘Alpha’. It did outperform previous generation C-Class catamarans [21].

Appendix D

Structured o-mesh

Due to the gap between the two profiles the mesh generation proved to be difficult. Many approaches were tried; to incorporate the gap in the structured O-mesh. Unfortunately all attempts resulted in meshes with very bad cells in critical areas. An attempt is shown below in figure D.1 highlighting some problem areas.

Also, to control a structured mesh generation many regions are required in which the mesh parameters are adjustable. Thus it requires a huge amount of time to generate additional geometries in order to guide the mesh generation.

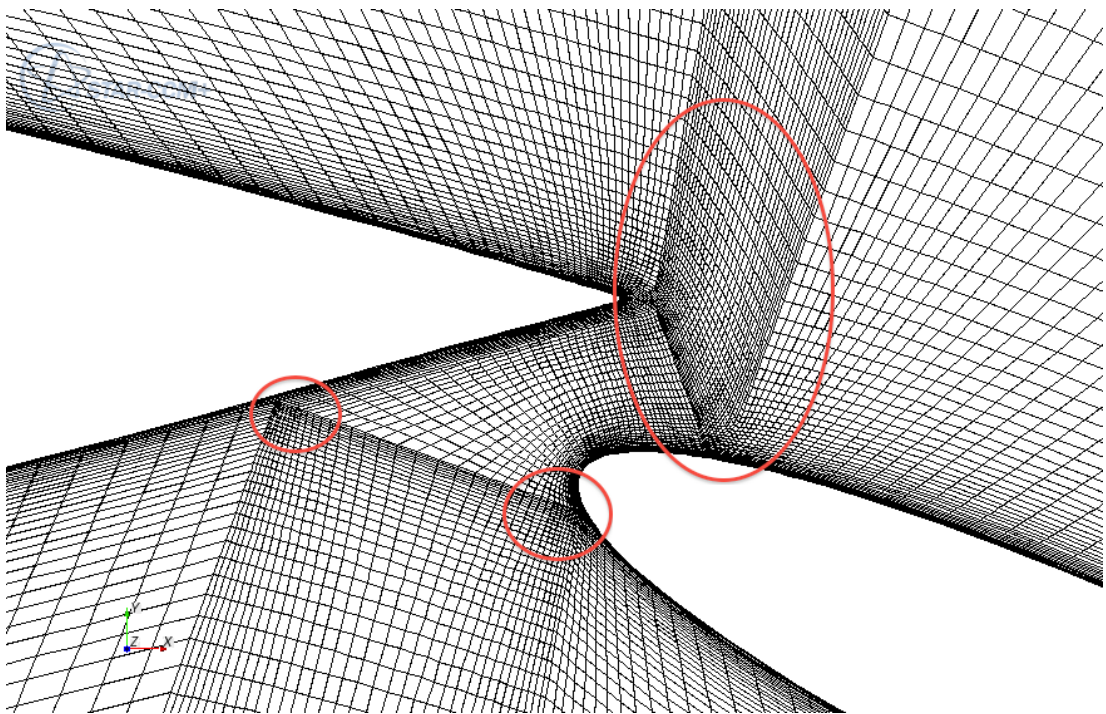


Figure D.1: mesh problems in the gap area due to a o-mesh around the two aerofoils

Appendix E

NACA 0012 profile results and analysis

The simulations of the NACA 0012 aerofoil were compared to experimental data. The experimental data was taken from a wind-tunnel test at a Re (Reynolds number) of 700×10^3 conducted in 1981 [37]. This is approximately the Re of a unit length aerofoil experiences at a velocity of 10 ms^{-1} at sea level.

$$Re = \frac{1.225 \times 10 \times 1}{1.7894 \times 10^{-5}} \approx 700000. \quad (\text{E.1})$$

The NACA 0012 profile was simulated with different meshes and two different turbulence models ($k - \epsilon$ model and SST $k - \omega$ model).

E.1 Mesh comparison

The experimental data was available for a full range of 180 degrees of $AoAs$ (Angle of Attack) in steps of 1° . According to the experimental data the stall is at 11° . The region of interest is the ‘linear’ lift region. To visualise how the meshes and turbulence models handle the linear lift region, pre and post stall, cases were run at 0° , 5° , 10° , 12° and 16° AoA .

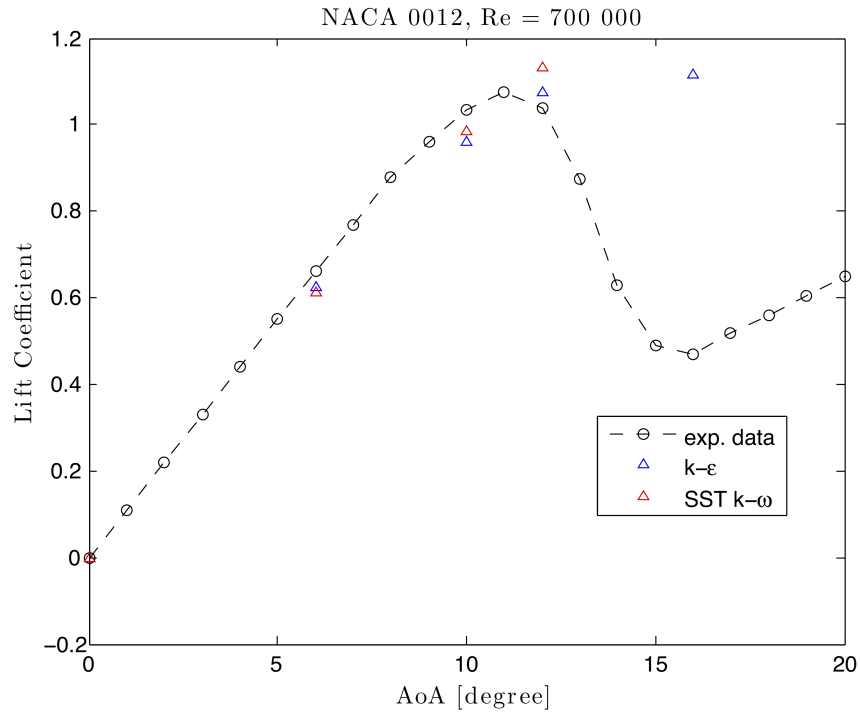


Figure E.1: Comparison of meshes and experimental data

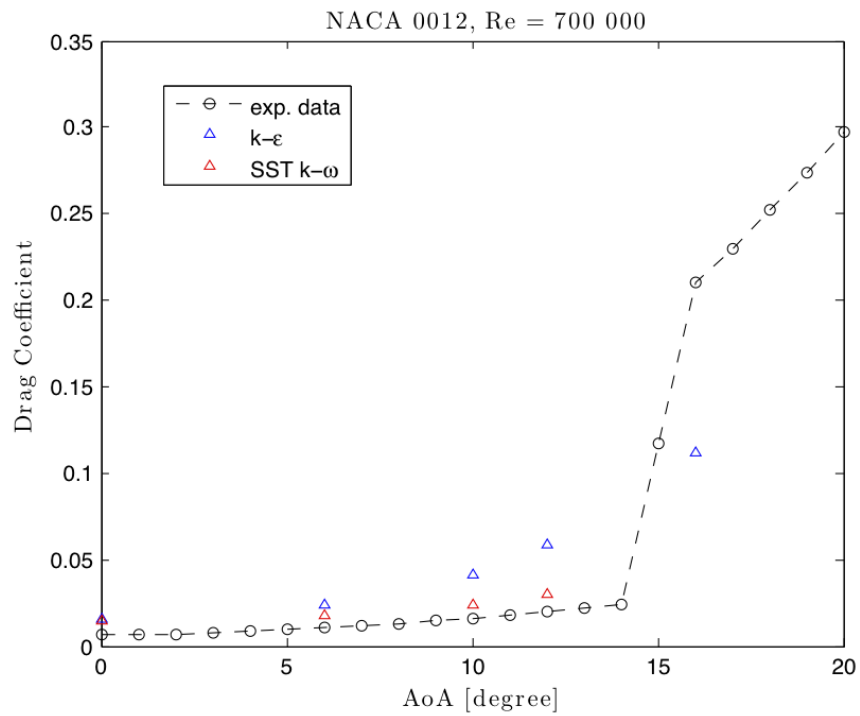


Figure E.2: Comparison of meshes and experimental data

The cases were run with numerous meshes. The results reached grid independence at the values shown in figures E.1 and E.2. The simulations run with the SST $k - \omega$ model did not converge for the cases at an AoA of 16° ; confirming the finding in the literature review that this model is not very robust with largely detached flows.

E.2 Turbulence model comparison

After running all cases of the wing with the flap, it was found that cases with high flap deflection suffered slow convergence and in some cases the residuals did not converge. To achieve convergence for cases with high flap deflection without re-meshing, the discretisation of the conservative equations were set to first-order upwind (as compared to the default second-order upwind).

To investigate the impact of using the first-order discretisation scheme on the result the two turbulence models were run with the first- and second-order discretisation for mass and momentum. The results are shown in figures E.3 and E.4 for C_l and C_d respectively.

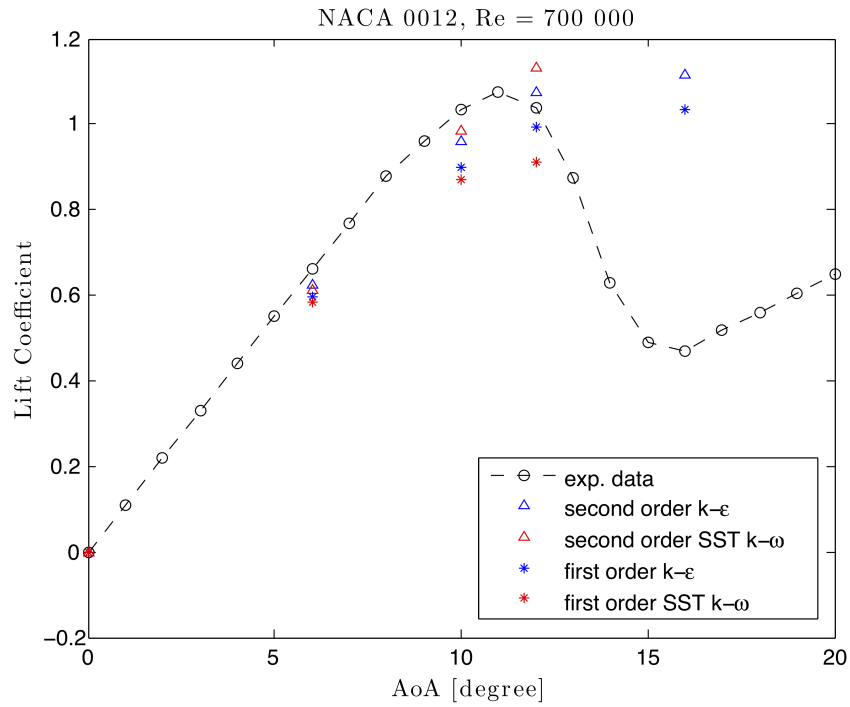


Figure E.3: Comparison of CFD data and experimental data

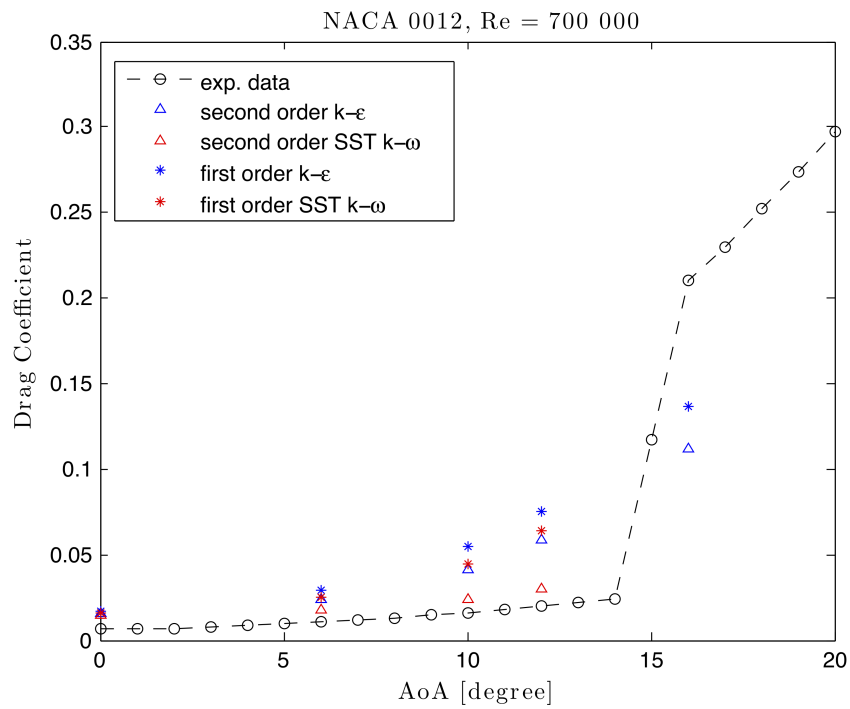


Figure E.4: Comparison of CFD data and experimental data

The simulations running the SST $k - \omega$ model did not converge for the cases at an AoA of 16° . This confirms the finding in the literature review, that this model is not very robust with largely detached flows.

E.3 Conclusion

The SST $k - \omega$ model with the second-order discretisation generally produces results closer to the experimental data than all the other simulations performed. This is especially true when comparing the C_d data from the SST $k - \omega$ model to the $k - \epsilon$ model (both with second order discretisation). However, when comparing the first-order results, the SST $k - \omega$ model under predicts the C_l values far more than the $k - \epsilon$ model close to stall.

The $k - \epsilon$ predictions are approximately as close to the experimental data as is the SST $k - \omega$ in the linear region (i.e. between 0° and 6°). In the linear region, the simulations under predict C_l by about 9% and over predict C_d by about 30%. In the stall region $k - \epsilon$ under predicts C_l more than does the SST $k - \omega$ but is much more consistent between the first- and second-order discretisation results. The SST $k - \omega$ performs poorly with first-order discretisation in this region and is more sensitive to the accuracy of the discretisation (for C_l and C_d).

The main requirement for the data is to predict C_l and C_d in the ‘linear’ region consistently with different flap deflections. Due to the convergence problems on the cases with high flap deflection (with second-order discretisation), it was decided to use only the $k - \epsilon$ -model since it produces data with much more consistency. Also this model proved to be much more robust in terms of convergence at high $AoAs$.

Appendix F

Simulation setup

With the assumptions made in the previous section the according selections are made for the physical modelling in 'STAR-CCM+4':

Category	Model
Dimensions	Two dimensions
Time	Steady
Material	Gas
Flow	Coupled
Equation of state	Constant Density
Viscous Regime	Turbulent
Turbulence	Reynolds-averaged Navier-Stoke
Reynolds-averaged turbulence	$K - \epsilon$ Turbulence
$K - \epsilon$ Turbulence Model	Standard $K - \epsilon$
K-Epsilon High y^+ wall Treatment	High y^+ Wall Treatment

Table F.1: selected physical models in the simulations

All models are used in their default configurations if not mentioned otherwise. The gas model has been adjusted to the environmental condition mentioned previously.

F.1 Explanation of choice of physical models

The 'STAR-CCM+ 4.04.011' manual advises to use the *coupled flow model* for incompressible flow if the computational resources are available [11]. The

advantages over the *segregated flow model* is that the number of iterations till convergence is independent of the mesh size, whereas the segregated approach requires more iterations with increasing mesh size.

The coupled flow solver solves the mass and momentum equations simultaneously.

The integration scheme was set to *implicit coupled solver*. The advantage over the *explicit coupled solver* is greater stability allowing a Courant number higher than unity. This resulting in higher local time steps, that can increase the rate of convergence. However this approach requires more storage.

The cases (in Appendix E) using the *SSTk- ω* model were set up in the same way, apart from the turbulence model selection.

F.2 Boundary condition

The boundary conditions were steep as following:

Region	Boundary condition
Domain	velocity inlet
Wing	'non-slip' wall
Flap	'non-slip' wall

Table F.2: Boundary conditions at the different regions

F.3 Initial condition

The initial conditions were kept to the default settings, apart from the ones mentioned below. The initial pressure was changed to the environmental pressure as referenced in section 3.5.1. The inflow velocity and direction was set to the final values, i.e. the velocity and AoA for the specific simulation.